U.PORTO

FEUP FACULDADE DE ENGENHARIA
UNIVERSIDADE DO PORTO

Semi-Automatic histology analysis of ovine pelvic tissues with 3D structural and quantitative analysis

Carolina da Ponte Rocha

DISSERTAÇÃO

July 2, 2018

Resumo

A histologia é uma técnica muito importante em investigação médica e no diagnóstico, uma vez que permite ter uma melhor perceção da arquitetura global dos tecidos. Permite obter informação acerca dos componentes presentes nos tecidos, ao contrário de qualquer outra técnica de imagiologia, como a tomografia computorizada ou a ressonância magnética. Devido à recente possibilidade de digitalizar lâminas histológicas, através de um digitalizador ou da aquisição de imagens recorrendo a câmaras acopladas a um microscópio, é possível obter imagens histológicas de toda a lâmina ou de apenas uma região de interesse. Isto faz com que surjam oportunidades de desenvolver algoritmos que vão auxiliar a análise de imagens histológicas, removendo um dos seu principais problemas, a subjetividade associada à experiência de cada patologista. As imagens histológicas também proporcionam uma forma de reconstruir o volume tridimensional de um dado tecido, permitindo a visualização do seu arranjo espacial.

O principal objetivo deste trabalho é automatizar procedimentos laboratoriais subjetivos e repetitivos em análise de imagens histológicas, através de uma série de algoritmos autónomos capazes de realizar essas mesmas metodologias e reconstruir, em 3D, um segmento de tecido usando essas imagens.

Sendo assim, foi desenvolvido um algoritmo para alinhamento de imagens, que vai permitir o alinhamento de um conjunto de imagens para a reconstrução 3D, e um algoritmo para separação de colorações e segmentação, para separar as diferentes cores presentes nas imagens e segmentar, posteriormente, a elastina e o colagénio. Os resultados para a segmentação automática, para 3 imagens diferentes, foram comparados com os resultados de uma segmentação manual feita por 10 pessoas de diferentes áreas, usando testes t pareados para a análise estatística. As segmentações manuais foram realizadas utilizando o ImageJ.

O algoritmo que foi desenvolvido para o alinhamento de imagens mostrou resultados satisfatórios. O desempenho dos algoritmos de segmentação foi avaliado através dos resultados dos testes t pareados para a segmentação de elastina (p=0.106, p=0.454 and p=0.584) e do colagénio (p=0.339, p=0.001 and p=0.600). A partir destes valores, é possível verificar que apenas um dos resultados, para a segmentação do colagénio, mostrou que a diferença entre a segmentação automática e manual foi estatisticamente diferente (p<0.050). A reconstrução 3D, por outro lado, originou reconstruções muito pouco exatas.

Em conclusão, os algoritmos foram desenvolvidos com sucesso e os resultados obtidos para a segmentação automática foram comparáveis ao resultados obtidos para a segmentação manual usando o ImageJ. Quanto à reconstrução 3D, existem algumas melhorias que podes ser introduzidas de forma a obter melhores resultados, como a diminuição da distância entre slices.

Abstract

Histology is a very useful technique in medical research and diagnosis since it gives a better understanding of the overall tissues architecture. It allows to obtain information about tissues components, unlike any other imaging technique, such as computed tomography or magnetic resonance. Due to the current ability to digitize histology slides, through scanner, or to acquire images through a camera connected to a microscope, it is possible to have histology images of the hole slide or just a zone of interest. This leads to an opportunity to develop algorithms that will help the histology analysis, removing one of the current problems, the subjectivity associated with pathologist expertise. Histology images also provide a way to reconstruct the three dimensional volume of a given tissue. The importance of the approach lays on the fact that it becomes possible to have a high resolution reconstruction of the tissue, allowing to see its spatial arrangement, as well as to have some other information, such as its volume.

The main objective of this work is to automate laboratory procedures that are subjective and repetitive in histology image analysis, by having a series of autonomous algorithms capable of performing those methodologies, and to reconstruct, in 3D, a tissue segment from the histology images.

Thus, it was developed an algorithm for image alignment, that allows the alignment of a set of images for the 3D reconstruction, and a stain separation and segmentation algorithms, to separate the different color that are present in the images and segment elastin and collagen, respectively. The results for the automatic segmentation, for 3 different images, were compared with manual segmentations performed by 10 people, from different backgrounds, using paired t-test for the statistical analysis. The manual segmentations were accomplished using ImageJ.

The developed algorithm for the alignment of the images showed satisfactory results. The performance of the segmentation algorithms was assessed through the results of the t-tests for elastin segmentation (p=0.106, p=0.454 and p=0.584) and collagen segmentation (p=0.339, p=0.001 and p=0.600). From this values, it is possible to see that only one of the results, for collagen segmentation, showed that the difference between manual and automatic segmentation was statistically different (p<0.050). The 3D reconstruction, on the other hand, originated inaccurate reconstructions of the tissues.

In conclusion, the algorithms were developed with success and the results obtained for the automatic segmentation are comparable to the results obtained from a manual segmentation using ImageJ. As for the 3D reconstruction, there are some improvements that can be made to assure better results, such as the decreasing of the spacing between slices.

Acknowledgments

I would like to express my deepest thanks to everyone that helped me and motivated me through these 5 years of hard work and during my master's thesis.

To Faculdade de Engenharia da Universidade do Porto for the education and providing the best conditions for my learning. To my supervisor, Professor Pedro Martins, for the guidance, support and experience during this work. To Rita Rynkevic for the help and providing some of the materials that was used during this project.

To my family for all the love, patience, support and incentive throughout these years, specially during the hard times. This would not have been possible without them.

To all my friends for the good moments that we had together and for standing by my side unconditionally.

Carolina Rocha

*" Intelligence without ambition
is a bird without wings. "*

Salvador Dali

Contents

List of Figures

List of Tables

List of Abbreviations

CT   Computed Tomography
DRR   Digitally Reconstructed Radiographs
LoG   Laplacian of Gaussian
MR   Magnetic Resonance
ROI   Region of Interest
VAT   Volume Adipose Tissue

Chapter 1

Introduction

1.1 Motivation and Challenges

Histology is the study of the microscopic structure of tissues and is a very important tool in medical research and diagnosis. The use of histological slides on medical diagnosis remains the "gold standard" for the diagnose of a large number of diseases, including almost all forms of cancer [10, 11, 12, 13]. Histological slides allow to get a better understanding of the disease, as well as to see all of its effects on tissues, since their assembly and preparation do not affect the overall tissues architecture.

Unlike other areas, such as radiology, where it is possible to conclude about the presence/absence of a disease and its spatial extent, histology introduces new information, as the grading [14, 15]. Considering cancer as an example, radiology will give information about the presence of lesions and its size/location. Radiographs have the advantage of being nondestructive, but their spatial resolution is low and interfere with a detailed analysis of tissue structure [16]. On the other hand, by analyzing an histological slide, it is possible to distinguish between different histological subtypes of cancer. Depending of the type of staining that is used, different tissue features can be highlighted.

Currently, histological analysis performed by a pathologist is the only method for the confirmation of presence/absence of a disease, or for the measurement of the disease progression. Regarding this issue, there have been some reported inconsistencies with the grading systems of some diseases, such as prostate and breast cancer [17]. Gleason scale is the most widely used method for grading prostate cancer, and it is based on architectural patterns. Studies have noticed some undergrading of Gleason scores five, six and seven (47%) and, to a lesser extent, eight, nine and ten (25%) [18]. There are also often mistakes on switching pattern two with three and pattern four with five. Thus, there is a hudge subjectivity on the diagnosis made by pathologists, since it can differ between pathologists and depend on their level of expertise [14, 13]. This fact emphasizes the need for automated methods to aid the analysis and classification of slides.

Recently, there has been an increasing of computed-aided diagnosis (CAD) techniques to histology image analysis, due to the ability of digitizing slides [19, 20]. This will enable pathologists

to focus on the more severe cases instead of focusing in all cases, including the ones that are obviously benign. About 80% of the prostate biopsies performed in the U.S. every year are benign [19], and 4 out 5 breast biopsies are negative for cancer [21]. Meaning that pathologists are spending about 80% of their time studying benign tissue, while they could be studying and documenting the mechanisms and consequences of diseases. There are several studies that shows a good diagnosis concordance (94%) between light microscopy and slide images based diagnosis [22, 23]. Discrepancies, most of the times, were due to the lack of pathologists expertise with virtual slides, and none of them caused clinical or prognostic implications.

Taking this into account, a need for a quantitative and qualitative analysis of histological images arises. This analysis will benefit either the diagnosis or the research: on the diagnosis, it would reduce/eliminate the inter and intra-observer variations and would also help understand the underlying reasons for a certain disease; on the research field, it would help understand the biological mechanisms of that disease.

Among all the possible analysis that can be performed in histology, it can be highlighted the quantification of collagen fibers. Collagen is the main component of the connective tissue, and its quantification is very useful to the characterization of several diseases [24]. The excessive production of collagen is present in some illnesses, such as lung fibrosis, liver cirrhosis and hypertrophic and keloid scars. On the other side, the loss of collagen is characteristic of diseases like rheumatoid arthritis and wound/ulcer damaged tissues [25, 26, 27].

During tissue repair and wound healing, the production of collagen is required to heal the damaged tissue [28]. The presence of collagen will determine the tissue function and ensure its structural integrity [29]. So, due to its central role in tissue healing, techniques for automatic collagen quantification are required.

Having histological slides digitized, it is possible to reconstruct the three dimensional (3D) histological volume. 3D histological analysis has the potential to be used for a better understanding of a disease growth pattern and spatial arrangement, and for the study of the biomechanical behavior of tissues [30]. It can have applications both in microscopic and macroscopic level [31]. For the microscopic level, it is used a magnification larger than 100 and it allows to obtain new and more precise histological and cytological parameters, in order to quantify physiological and pathological phenomena. At the macroscopic level, it is possible to analysis tissue structures that are too large to be analyzed on 2D but, at the same time, too small to be dissected.

A three dimensional histological analysis also allows to visualize, in a easy way, the 3D shape and volume changes of the tissue. It can be used to investigate and validate new techniques and algorithms in volumetric medical imaging. Volumetric medical images (magnetic resonance (MR) and computed tomography (CT), for example) are 3D data sets of a sequence of 2D data slices [32]. However, usually due to the large amount of collected data, those images have to be compressed in order to efficient transmitted, causing the reduction of quality. With histology volume analysis it is possible to create high resolution atlases of different organs and study their structure and spatial relation of the different cell features [33].

Considering this information, this work will focus the development of an autonomous algorithm for the alignment of images and the segmentation of some tissue components, such as collagen and elastin. Further, those images, after segmented and aligned, are going to be used in the three dimensional reconstruction of the tissue.

1.2   Document Outline

On the next two chapters are described the state of the art and literature review of algorithms for histological image analysis (Chapter 2) and methodology for the three dimensional analysis (Chapter 3). In Chapter 2, there are described some algorithms for image alignment, image segmentation and stain separation. Chapter 3 includes an overview of some of the techniques and software used for the three dimensional reconstruction, segmentation and tissue quantitative analysis. In Chapter 4, it is described the methodologies and algorithms that were developed for this purpose. Chapter 5 presents the results and discussion for each of the developed algorithms and used methodologies. Finally, in Chapter 6 are described the main conclusion and future work.

Chapter 2

Histological Image Analysis

In this chapter, a literature review on algorithms for image alignment, stain separation and image segmentation will be done. It will be described the main ideas of each class of algorithms, as well as some of the already developed algorithms for this purpose.

2.1 Image Alignment

The ultimate goal of image alignment, also referred as image registration, is to align images with respect to each other. One of the images, the one that is already aligned, is called reference image, and the image to be aligned with respect to the reference image is called sensed image [1]. On the medical field, image alignment methods allow to combine different images (acquired from different modalities), in order to merge important information and, this way, facilitate patient's diagnosis [34]. Besides improving the diagnosis, these methods are also used for planning treatment, guiding treatment, creating models of anatomy and monitoring disease progression [35, 36]. In the research area, image registration is used to understand diseases processes and evolution.

There are several classifications for image alignment algorithms, as shown in Fig. 2.1. These algorithms are grouped based on their criteria. On the next sections, a description of each of the groups is presented.

2.1.1 Dimensionality

Concerning the dimensionality, methods for image registration can be classified as spatial or time-series [37]. As for the spatial dimensions, algorithms are categorized based on the geometric dimensions of the images that are involved on the alignment:

- **2D-to-2D** - In this case, both images are 2D images, and they can be aligned by performing just one rotation and two translations. 2D-to-2D registration is the simplest and more used method of this group, despite of being inaccurate [38].

- **3D-to-3D** - Images used in 3D-to-3D registration are 3D images only. This kind of methods assume that there are no distortions on the internal anatomy of the patient and the spatial

Classification Criteria for Image Alignment Methods	Dimensionality
	Registration Basis
	Nature of the Transformation
	Transformation Domain
	Interaction
	Modalities
	Subject
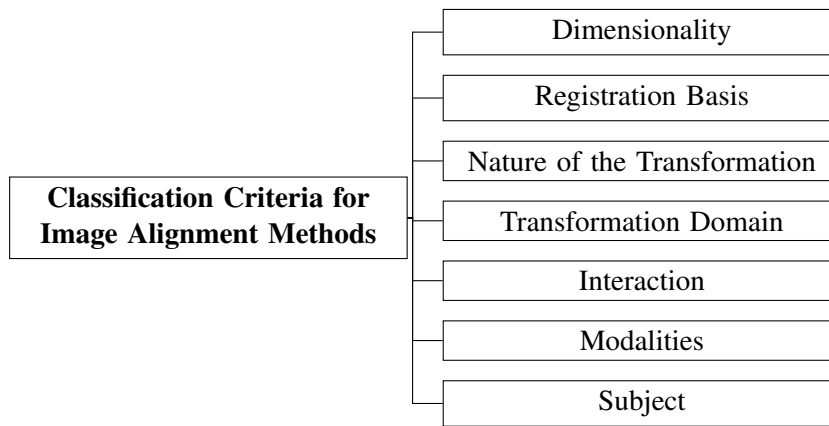
Figure 2.1: Classification Criteria for Image Alignment Methods [1].

relationships between organs do not change [37]. Either this method, or the 2D-to-2D registration can be accomplished by the extraction of landmarks that are used for the matching between both images [39].

- **2D-to-3D** - This type of image alignment algorithms perform the alignment of 2D images with 3D images. 2D-to-3D image registration can be used in image guided radio-surgery, where it is crucial to detect any changes in patient position between the planning of the surgery and the surgery itself. It is used X-ray images taken during the procedure and the preoperative computed tomography (CT) scan. To align those images, it is often generated digitally reconstructed radiographs (DRR) from the CT scan to be used as reference images [40, 41, 42]. X-ray images, captured in real time, are, then, compared with those reference images to detect any changes. The alignment between the DRRs and X-ray images is accomplished by the extraction of image features or based on image intensity. There is also some literature that suggest the creation of DRR of X-ray images instead [43].

If the variable time is added to the images that are going to be aligned, the registration is classified as time-series registration. This is applied when several images, from the same patient, for example, are acquired in order to conclude about the progression of a disease.

2.1.2 Registration Basis

The registration algorithms under this criteria can be classified as intrinsic or extrinsic, depending on the methodology used to find the interest areas for the matching [1]. The extrinsic methods comprises the introduction of external objects into the image space, so that they are easily detected by the algorithm. These methods have the disadvantage of requiring additional spatial information, from a different source, in case the image has low resolution. In opposition, in the intrinsic methods only the information that are present on the image is used for the alignment. Depending on the used information they can be classified as [37]:

- **Feature-based Methods** - Those features can be the image gradient, image skeleton, contour, segmented objects, or geometric objects such as edges, corners or surfaces [44, 45, 46]. The alignment is done by matching the landmarks of the sensed image and the landmarks of the reference image. It is a versatile method once it can be applied to any type of images. However, the success of the registration depends on the success of the feature extraction phase, and a robust and automatic feature extractor is difficult to archive. The main advantage of these algorithms is the possibility of a fast computation, nevertheless since, most of the time, it is only extracted a few objects, the accuracy may be compromised [40].

- **Segmentation-based Methods** - Segmentation-based methods can be rigid or deformable [1]. The rigid methods extract the same objects from both images and use it for the alignment. As for the deformable methods, an object is extracted from an image and is elastically deformed to fit the reference image. The segmentation is usually accomplished with deformable models such as snakes or active contours (2D), or nets (3D) [47]. The deformable models grow iteratively and stop when the optimization criteria is met. Rigid methods are less complex than deformable methods. As segmentation has low computational complexity, segmentation-based methods are very used methods for image alignment. Registration based on rigid methods are usually applied to intrasubject registration and the deformable methods to intersubject registration.

- **Intensity-based Methods** - Uses directly the gray-level values of the images for the matching. There are two different approaches: reduce the gray value content to a representative set of scalars and orientations, or use the full image content [1]. However, intensity-based methods can lead to some mistakes, once intensity similarity does not mean anatomical similarity [44]. The reduction of the gray value content can be done with the computation of the first order moments, in order to obtain the center of gravity and main orientations of the image. The registration is accomplished by aligning the gravity centers and principal orientations of both images. This method shows some lack of accuracy due to the fact that it is not capable of dealing with volume changes. Still, as it is easy to implement, it is often used when accuracy is not the most important parameter. Full image content methods, on the other hand, use all the available information of the image, without reducing it. Some of these methods include: cross-correlation, fourier-domain-based cross-correlation, phase-only correlation, mutual information, minimization of the absolute or squared intensity differences, or minimization of variance of gray values within segments [48, 49, 50].

2.1.3   Nature of the Transformation

A transformation can be rigid, affine or elastic. These transformations are useful to move the sensed image in a way that it overlaps the reference image. An affine transformation combines translations, rotations and scaling. Rigid transformations are a special case of affine transformations, where only translations and rotations can occur. Both rigid and affine transformations can

Figure 2.2: Matrix definition for each type of transformation, where δ_x and δ_y describe translations in the x and y axis, θ is the rotation angle and α_x and α_y are scaling factors. Adapted from [2].

be represented by a matrix equation, such as Eq. 2.1 [1]. Variables y and x are the new and old coordinate vectors, respectively.

$$y_i = a_{ij}x_j \tag{2.1}$$

Matrix a_{ij}, presented in Eq. 2.1, is used to define the transformation. In Fig. 2.2, are shown the used matrices for each transformation.

Affine transformations preserve the parallelization and intersection between lines. If angles between the lines are also preserved a similarity transformation (another special case of affine transformation) has occurred. Finally, there is a perspective projection transformation if line properties are not preserved.

Elastic methods are methods that allow to register images in a more flexible way, by spatially variant local warping [2].

2.1.4   Transformation Domain

A transformation can also be classified as global if it is applied to the entire image, or local if only applied to a section of the image.

2.1.5   Interaction

Concerning the user interaction, algorithms for image alignment can be automatic, interactive or semi-automatic [37]. Automatic algorithms only have to be fed with the images, in order to obtain the results. In opposition, in interactive algorithms, the user has to align the images manually, with the help of the software. Finally, in semi-automatic algorithms, the user usually has to initialize the algorithm by, for example, performing the segmentation of objects, or to accept or reject the alignment results.

There is a trade-off between the minimization of the user interaction and the speed, accuracy and robustness of the algorithms[1]. With user interaction, it is possible to narrow the search

area of target objects to help the alignment, or refuse the result in case there is a mismatch of the images. However, with interaction it is more difficult to validate an algorithm, once the level of interaction is hard to quantify.

2.1.6 Modalities

The registration algorithms can be grouped as mono-modal, multi-modal, model-to-modality or modality-to-model, depending on the types of images that are used for the alignment [37]. On mono-modal applications, both images belong to the same modality, while on multi-modal applications, images come from two different modalities. In the remaining two cases, only one image is used on the registration process. The other "modality" is composed by anatomical or physiological models.

Multi-model registration methods can provide useful complementary information that is very helpful in patients diagnosis. This technique can be useful as it can combine X-ray images with overlays of previously acquired magnetic resonance images (MRI), so that real time tracking of the X-ray images can be added to the anatomical context given by the MRI [51]. Although, their alignment can be hard to archive, due to the fact that images from different modalities may have different intensity mappings, and structures that are captured in one technique may not be captured by the other [52, 53]. Mono-modal methods can be applied, for example, for monitoring the growth of certain structures, verifying interventions and subtraction imaging.

2.1.7 Subject

Image alignment methods can be classified as intrasubject, intersubject or atlas. Intrasubject methods concern the methods in which images belong to the same patient. It brings information about the evolution of a disease, once it is possible to align images taken in different times [35]. Image registration algorithms are considered intersubject if the images belong to different patients. It is usually used to compare patients with healthy people [35] or to compare sizes and shapes of anatomical structures. Finally, it is atlas if one image belong to one patient and the other is from a database. That database include representative images for the class of the image that is used on the alignment. It is a very useful technique for three dimensional visualization, treatment planning and evaluation, surgery planning, and image-assisted surgery. The main idea is to recognize objects in the patient image by aligning it with the reference image [54].

2.1.8 Image alignment Algorithms

The remaining of this section will discuss some algorithms present on the literature concerning the alignment of 2D images, which are the type of imges used in this work.

Conlin et al developed an algorithm that uses the Hough Transform of edge maps to align MR images [3]. The alignment is done based on one of the kidneys. First, it is generated an edge map for one of the MR images, using the Canny edge detector. After obtaining the edge map, the user selects the kidney contour, which is going to be used as a template for the alignment. Second,
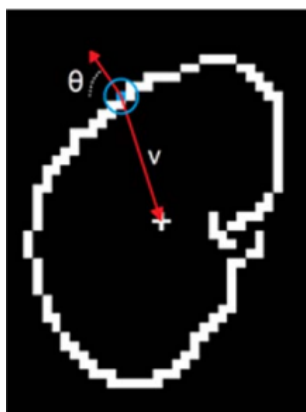
Figure 2.3: Kidney contour obtained from the edge map. Each pixel is associated with an orientation and a vector. Adapted from [3].

using the Hough Transform, it is computed, for each pixel of the contour, its angle (θ), that defines the orientation of the contour on that zone, and its vector (υ), that points to the pixel of the center of the contour, as shown in Fig. 2.3. It is generated a table with the angle and vector for every pixel of the image. Next, to align a new image with respect to this template, it is generated its edge map using again the Canny edge detector. However, this edge map will contain the kidney edge as well as all the other edges of the image. Lastly, for each edge pixel it is calculated its orientation and, if the orientation matches any of the orientations present on the table, the correspondent υ is used to point to the center of the contour. The location to where more vectors are pointing will be the true location of the kidney. Images are aligned based on the center displacements, using the affine transformation.

Wei-Yen Hsu came up with another feature extraction based algorithm for image alignment [55]. Feature extraction is an important task in image registration techniques, once it influences the accuracy of the algorithm. For the feature extraction, in this case, it is used wavelet-based edge correlation, in which are extracted feature points with strong and consistent responses under different scales. There were used 2D wavelet transforms as two 1D wavelets in x an y directions, represented in Eq. 2.2 respectively [55], where S(x,y) are smoothing functions.

$$
\begin{aligned}
\varphi^H &= \frac{\partial S(x,y)}{\partial x}, \\
\varphi^V &= \frac{\partial S(x,y)}{\partial y}
\end{aligned}
\tag{2.2}
$$

Wavelet transforms are computed for several different scales using Eg. 2.3.

$$
\varphi_j = \frac{1}{2^{2j}} \varphi\left(\frac{x}{2^j}, \frac{y}{2^j}\right)
\tag{2.3}
$$

These wavelets are used to calculate the gradient of the image for multiple scales and, consequently, its modulus. The local maximums of the modulus of each scale corresponds to the edge

points. To increase the accuracy of this extraction, it is used a edge correlation method to filter all the noise through a multiscale edge confirmation, represented in Eq. 2.4, where M is the modulus of the gradient for a given scale and f(x, y) is the image. Only points that are detected in all scales are kept at the end of this algorithm, eliminating the noise.

$$C_n(j,x,y) = \prod_{i=0}^{n-1} M_{j+1} f(x,y) \tag{2.4}$$

The registration process is done by an analytic differential approach, whose main goal is to minimize the energy function, present in Eq. 2.5.

$$E(M,T) = \sum_{i=1}^{H} \sum_{j=1}^{K} m_{i,j} \left\| u_i - v_j T \right\|^2 - \alpha \sum_{i=1}^{H} \sum_{j=1}^{K} m_{i,j} + \beta \sum_{i=1}^{H} \sum_{j=1}^{K} m_{i,j} \log m_{i,j} + \lambda trace \times \left[(T-I)^t (T-I) \right]$$

$$\tag{2.5}$$

The data sets that represent the extracted points from each image is written as u_i and v_j, the mapping between them is represented by matrix M, consisting of $m_{i,j}$, and T is the geometric transformation. The first term of Eq. 2.5 is the error term. The second is used to avoid excessive null correspondence (the larger the α the less point are considered to be outliers). The third term is an entropy function that assures that matrix M do not contain negative numbers. Finally, the last term is a constraint to the transformation function.

2.2 Analysis Algorithms

Histological staining contains, most of the times, different types of colors due to the fact that different components of the tissues needs different dyes. These mix of colors provides truly important information about tissues composition, unlike any other tissue imaging technique such as radiology, for example. However, this can also be disadvantageous, namely on the quantification of a particular tissue component [4] or on a qualitative analysis [56]. As such, the analysis on the microscope results on the visualization of a mix of all the colors that were used, which can lead to the loss of information [57]. Thereby, appear some algorithms such as Stain Separation algorithms, that allows to separate these colors in a way that is possible to obtain information about each one of them in a separate way.

2.2.1 Stain Separation Algorithms

2.2.1.1 Color Deconvolution based algorithms

The color deconvolution algorithm was first proposed by Ruifrok and Johnston [57]. This algorithm allows to separate the different colors used on a given histology, even if they overlap in the spectrum.

The relative intensity of each RBG channel of a given image depends on the concentration of stain in a non-linear way [58]. Therefore, it cannot be directly used on the separation of each stain

present on the image. However, the optical density for each RGB channel can be calculated by the following equation [57]:

$$OD = -\log \frac{I}{I_0} = A \times c_c \tag{2.6}$$

where I is the light that goes through the sample, I_0 is the incident light and A is amount of stain with absorption factor c.

It is assumed that the optical density of each RGB channel is linear with the concentration of the absorbed material, allowing it to be used for the separation of the different colors present on the sample.

It is defined, for each staining used on the histology, a 1 by 3 vector (stain vector), where every column corresponds to the optical density for each RGB channel. These values can be determined through the measurement of the relative absorption of red, green and blue on blades with only one staining present [59]. Combining those different vectors originates a matrix, where each line corresponds to a different staining, as shown on the following matrix:

$$\begin{bmatrix} od_{11} & od_{12} & od_{13} \\ od_{21} & od_{22} & od_{23} \\ od_{31} & od_{32} & od_{33} \end{bmatrix} \tag{2.7}$$

Finally, it is determined an orthonormal transformation of the RGB information to get an independent information about the contribution of each one of the stainings. Matrix present on Eq. 2.7 is normalized and inverted, and then multiplied by the image optical density, in order to obtain the orthogonal representation of the stains.

Similar to this color deconvolution algorithm is the method described in [60], where the authors describe a way of finding the stain vectors. Those vectors are found based on a specific geodesic direction, that is, the shortest path between two unit-norm color vectors on a sphere. This direction is determined by projecting the OD pixels on a plan formed by the two largest vectors of the singular value decomposition of the OD pixels.

2.2.1.2 Automated Algorithms

More complex methods have been developed along the years. Tadrous suggested an automated algorithm for the separation of an image on it's components [4], as shown in Fig. 2.4. This algorithm determines a mask of the representative portion of the stained tissue, by thresholding on the saturation image. Then, it takes a single channel of the RGB image (the one that gives the majority of the contrast of the component of interest) and inverts it. This inverted channel is weighted and added to each original channel, separately, in an iterative process with the goal of finding α (value for weight the chosen channel). The constant α is found when the minimum variance within the mask is reached. The combination of the modified channels gives the de-stained image.
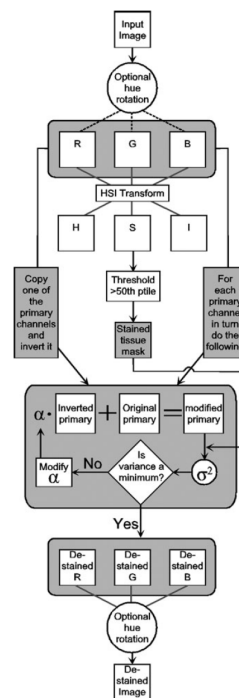
Figure 2.4: De-staining algorithm. Adapted from [4].

Wand et al [61] developed a method for an automated segmentation and classification of tumor tissues from microscopic images, based on the color of the image pixels. This method comprises three distinct phases: color normalization to avoid the situation where the same set of images have different illumination distribution; automatic feature extraction in order to select automatically the training samples; and principal component analysis (PCA) as a learning algorithm.

2.3 Image Segmentation Algorithms

Image segmentation has the objective of dividing the images into regions, which usually correspond to an object or part of an object. Pixels within a region have similar attributes.

In the medical field, image segmentation allows to perform shape analysis, detect volume changes and make a precise radiation therapy treatment plans. It facilitates the extraction of meaningful information to help on the patients diagnosis [62]. However, in some cases, it is still difficult to obtain accurate results, due to cluttered objects, occlusion, image noise, nonuniform object texture or lack of edges (caused by deficiencies in image contrast), for example [63].

Image segmentation techniques can be classified in three main categories (Region-Based Methods, Edge-Based Methods or Neural Networks), as shown in Fig. 2.5 [5]. The next few sections will focus the explanation of each group of methods present in Fig. 2.5
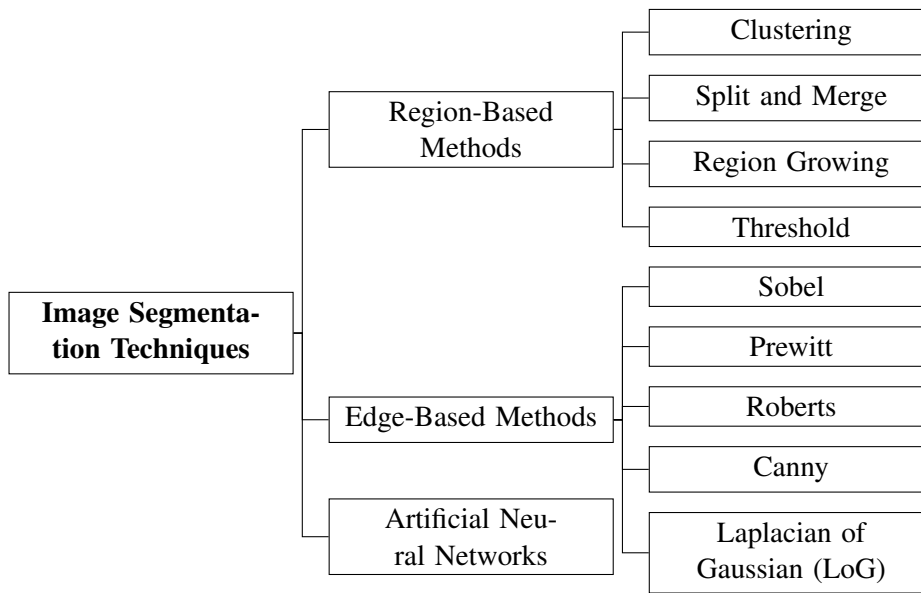
Figure 2.5: Classification of Image Segmentation Methods [5].

2.3.1 Region-Based Methods

Region-based methods for image segmentation divide the images into regions, grouping pixels with the same intensity values.

- **Clustering** - Clustering is the process of partitioning data into distinct clusters. Objects that belong to the same clusters are similar, while objects from different clusters are different, considering their attributes.

  K-means algorithm starts by defining K centroids at random positions [64, 65]. Each new point, of a given sample, is associated with the closest cluster, depending on the euclidean distance between the point and the centroids of all that cluster. This way, for each iteration, it is computed this distances, and the point is considered a member of the closest cluster. At the end of each iteration, the centroids are recalculated. This algorithm stops if the clusters composition do not change between iterations. K-means algorithm is very efficient, unless the input is a large amount of data, which increases considerably the computational cost. In addiction, the obtained clusters, at the end of the algorithm, depend on the initial centroids.

  Fuzzy C-means algorithm, unlike K-means algorithm, allows the same point to belong to several clusters at the same time [66, 67]. Each point contains a membership value related to its similarity to the clusters. Those membership values are numbers between 0 and 1, and the sum of all membership values for one point must be equal to 1. The higher the similarity of a point to a cluster, the closest to 1 the membership value is for that cluster. This algorithm is also iterative and, in each iteration, the centroids position are updated as well as the membership values. At the end of the algorithm, defuzzification is applied to decide the final clustering.

- **Split and Merge** - Split and merge segmentation algorithms subdivide images in successively smaller subregions (called superpixels), so that a predicate, defined by the user, is verified in that subregions [6, 68]. A predicate can be, for example, pixel intensity. The image is divided in smaller regions while the predicate, for that region, do not verify. At the end of the splitting algorithm, there are, normally, adjacent subpixels with similar properties. Thus, the merging algorithm is used to merge adjacent regions that, if merged, continue to verify the predicate [69].

- **Region Growing** - Region growing is a technique that groups pixels or subregions into larger regions, based on some criteria [70]. The process starts with a set of "seed" points that grows into larger regions by appending the neighborhood pixels if they meet the growing criteria, in other words, if their properties and the neighborhood pixels properties are similar (color, for example). The "seed" points can be defined by the user or can the defined automatically by an algorithm [6].

- **Threshold** - Thresholding consists on classifying a given pixel according to its intensity being higher/lower than a value (threshold value). Alternatively, it can be chosen an interval, being the region of interest with the intensities part of that interval. The threshold value is chosen based on the intensities of the target region. Thresholds can be global, local or dynamic, depending if it is the same to the entire image, just to a part of it (being its values dependent of the neighborhood pixels) or if it depends to the spatial coordinates, respectively [6].

2.3.2 Edge-Based Methods

Edge-based methods for image segmentation are used to find discontinuities in intensity values. This edges are usually computed through the gradient of the image (first order derivatives), Eq. 2.8, or through the Laplacian (second order derivatives), Eq. 2.9 [6].

$$\nabla f = \begin{bmatrix} g_x \\ g_y \end{bmatrix} = \begin{bmatrix} \frac{\partial f}{\partial x} \\ \frac{\partial f}{\partial y} \end{bmatrix} \tag{2.8}$$

$$\nabla^2 f(x,y) = \frac{\partial^2 f(x,y)}{\partial x^2} + \frac{\partial^2 f(x,y)}{\partial y^2} \tag{2.9}$$

2.3.2.1 Edge Detectors

- **Sobel** - The Sobel edge detector (Fig. 2.6) approximates the first order derivatives to differences between rows and columns of a 3-by-3 neighborhood. After applying Sobel, a pixel is considered an edge pixel if its value is larger than a threshold value [71].

- **Prewitt** - Prewitt edge detector is similar to Sobel, as can be seen in Fig. 2.6. However, the results shown by this filter are noisier [72].

- **Roberts** - Robert edge detector approximates the first order derivatives to differences between adjacent pixels (Fig. 2.6). It is the simplest detector [73].

- **Canny** - The Canny edge detector is the most used edge detector and it is typically implemented as follows: smoothing of the image using a Gaussian filter, with a specific σ, to reduce noise and some image detail; computation of the gradient magnitude and orientation for each pixel; label a pixel as edge if its gradient magnitude is larger than the magnitude of its neighborhood pixels (in its gradient orientation); weak edges are removed by hysteresis thresholding [74]. In hysteresis thresholding, pixels above the threshold are kept, pixels below the threshold are eliminated, and pixels between the values of the high and low thresholds are kept just if they are connected to already classified edges.

- **Laplacian of Gaussian (LoG)** - The Laplacian of Gaussian (LoG) filter is defined as [6]:

$$\nabla^2 G(x,y) = \frac{\partial^2 G(x,y)}{\partial x^2} + \frac{\partial^2 G(x,y)}{\partial y^2} \qquad (2.10)$$

where, G(x,y) is the Gaussian function. The Gaussian function is represented in Eq. 2.11.

$$G(x,y) = e^{\frac{x^2+y^2}{2\sigma^2}} \qquad (2.11)$$

The Gaussian function performs the smoothing of the image by a factor σ. The LoG filter computes the second derivative of this function, which leads to the determination of the image edges.

2.3.3 Artificial Neural Networks

Artificial neural networks are computational models inspired by the nervous system. These networks can acquire and store knowledge and are defined as a group of processing units (neurons) connected by synapses (usually matrices and vectors) with different synaptic weights [7].

Applications based on neural networks have some key characteristics: capability to adapt from experience (with the increase of information that is processed, the network parameters - synaptic weights - are adjusted), learning capability (through the chosen learning method, the network can extract the relationship between the variables), generalization capability (after learning the behavior of a process, it is possible to apply it to unknown information) and distributed storage (the knowledge is stored on the synapses, which increases the robustness in case one of the neurons is lost).

Figure 2.7 summarizes the model for the artificial neuron. The input signals (x_1, x_2, ..., x_n) are signals or samples that come from the environment and represent the values of the variable used on the neural network. Each sample is multiplied by its weight (w_1, w_2, ..., w_n), based on its relevance for the neuron. All input signals, after weighted, are aggregated, in the linear aggregator

-1	-2	-1
0	0	0
1	2	1

-1	0	1
-2	0	2
-1	0	1

Sobel

$g_x = (z_7 + 2z_8 + z_9)$
$\quad - (z_1 + 2z_2 + z_3)$

$g_y = (z_3 + 2z_6 + z_9)$
$\quad - (z_1 + 2z_4 + z_7)$

-1	-1	-1
0	0	0
1	1	1

-1	0	1
-1	0	1
-1	0	1

Prewitt

$g_x = (z_7 + z_8 + z_9)$
$\quad - (z_1 + z_2 + z_3)$

$g_y = (z_3 + z_6 + z_9)$
$\quad - (z_1 + z_4 + z_7)$

-1	0
0	1

0	-1
1	0

Roberts

$g_x = z_9 - z_5$
$\quad\quad g_y = z_8 - z_6$
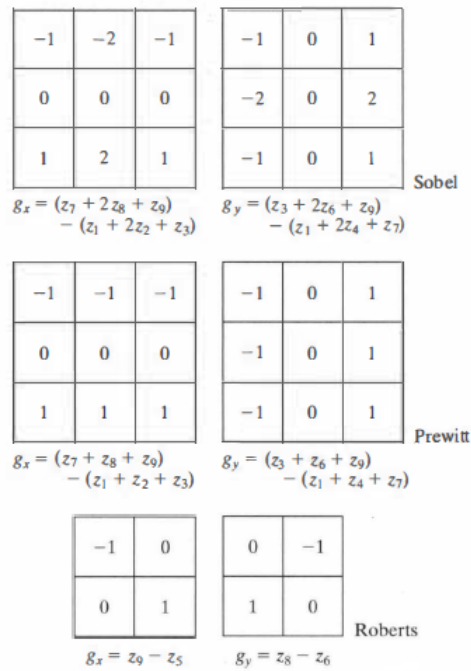
Figure 2.6: Edge detector filters. Adapted from [6].

(Σ), and added to the bias (θ) to produce the activation potential (u). If $u \geq \theta$, the neuron produces an excitatory potential. Equation 2.12 shows how to calculate the activation potential.

$$u = \sum_{i=1}^{n} w_i x_i - \theta \tag{2.12}$$

The output signal (y) produced by the neuron is given by the u and is restricted within a range of values (consequence of the activation function g). This output is used as input for other neuron of the network.

$$y = g(u) \tag{2.13}$$
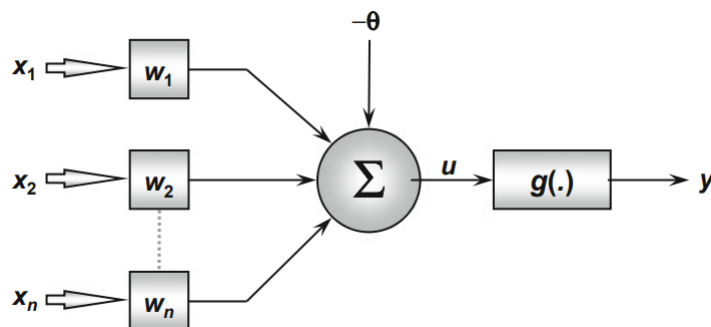
Figure 2.7: Representation of an artificial neuron. Adapted from [7].

Neural Networks can be applied in several areas such as pattern recognition/classification, data clustering, prediction system and system optimization.

Chapter 3

Three dimensional histological analysis

In this chapter, an overview of the three dimensional histological reconstruction techniques, from the tissue preparation to the used algorithms for the images registration, is addressed. Methods for tissue segmentation using Mimics are referred later and finally, the quantitative analysis will be described.

However, since this pipeline is going to be accomplished using the software Mimics [75], details about each existing algorithm will not be described.

3.1 Three dimensional histological reconstruction

Three dimensional histological volume reconstruction has the potential of providing important information for a quantitative and comparative analysis and assessment of pathological finding in volumetric medical imaging [76]. Three dimensional confocal two-photon microscopy, which allows cellular imaging with several hundred microns deep in various organs [77], can provide high resolution cell morphology but only at a local extent (limited field of view). Histological reconstruction provides information over a larger spatial extend [31].

This reconstruction can be obtained by concatenating a set of 2D histological images. Those bidimensional images are obtained from anatomical structures that are fixed using paraffin embedding or cryogenization [31]. Then the anatomical structure is trimmed into thin sections, with a constant thickness and inter-gap interval. Each section is assembled into slides and digitized with a digital camera or scanner. It may be introduced some guides on the tissue before the fixation phase in order to have reference points to be used by the software for the 3D reconstruction.

However, there are some errors that can be introduced into the phase of tissue preparation that can affect the success of the three dimensional tissue reconstruction, namely the registration phase: during the preparation of histological sections some distortion can appear due to shrinkage, expansion, tears and folds on the tissue [76], and when laying the cover-glass it can appear some spots, leading to artifacts; and during the sectioning the edges of the tissue can become deformed, and consequently deform the whole section [78]. During the image acquisition phase there can be problems with the non-uniform illumination that come from the camera used for the acquisition.

The tissue reconstruction starts with a rough pre-alignment phase, followed by a finer histology registration (intra-histology refinement), to smooth the irregular slide-to-slide transitions produced by the pre-alignment algorithms. Pre-alignment can be done by registering slides to an external reference (histology-reference pre-alignment) or registering slides to each other (intra-histology pre-alignment). The registration method used after this techniques can include: rigid, affine, 1D piecewise linear, elastic spring triangular mesh, discrete smooth interpolation, displacement field, curvature flow, symmetric normalization (SyN) diffeomorphism, diffeomorphic inverse consistent algorithm, large deformation difeomorphic metric mapping (LDDMM), or tensor-product B-spline [79].

There are also some algorithms that do the tissue reconstruction without external references, and are used in software like Voloom (microDimensions GmbH), BioVis3D, or 3DView (3DHIS-TECH Ltd.) [79]. These approached are more likely to have geometric artifacts, such as the straightening of curvatures, false z-axis orientation, the conversion of asymmetric shapes into symmetric, wobbly boundaries, and drift or z-shift effect caused by the accumulation of correlated registration errors ones [80]. Nevertheless, this type of registration is useful in case external references are not available, if the exact shape of the reconstruction is not very important, or if maximum alignment (shape that comes from a alignment that cannot be improved) coincides with the true shape.

There are already some applications of this technique to breast cancer, namely on the reconstruction of ductal carcinoma *in situ* (DCIS) from virtual slides [81]. They created a methodology for the 3D reconstruction of the DCIS. The main goal of this study is to increase the understanding of the biology of the ductal carcinoma *in situ* in 3D and its relationships to invasive disease. Besides, they also wanted to help people recognize dangerous DCIS (DCIS with a high chance of progression) from a relatively safe DCIS. Another approach is used in prostate cancer, where after a radical prostatectomy, an hispathologic analysis is performed in order to acquire knowledge about this type of cancer [82]. Prostate is sectioned into 3-4mm thick slides that are aligned and registered by the affine and elastic registration methods. After, the information obtained from the 3D histological reconstruction was compared with the 3D reconstruction of the transrectal ultrasounds. There is also another study focusing a 3D reconstruction of brain volume of rats from immunohistochemically stained histology images, that is after registered with the correspondent 3D magnetic resonance image to study the rodent stroke model [83]. The combined histological and MRI reconstructions allows to understand how changes in MR signal intensity in the stroke lesion correspond to microscopic histological changes. This can also be useful to study the neurobiological foundations of signal changes in MRI.

This reconstruction can be accomplished using the software Mimics, by Materialise [75]. Mimics is a software used for 3D design and modeling that can create 3D models from stacks of 2D images. In alternative, there is Voloom by microDimensions [8]. Voloom is a software specialized in automated 3D histology reconstruction, visualization, and analysis in digital pathology. In Fig. 3.1 there is an example of a 3D reconstruction of mouse tissue using Voloom.

Due to the lack of available information on this topic, in Fig. 3.2 there is an example of a
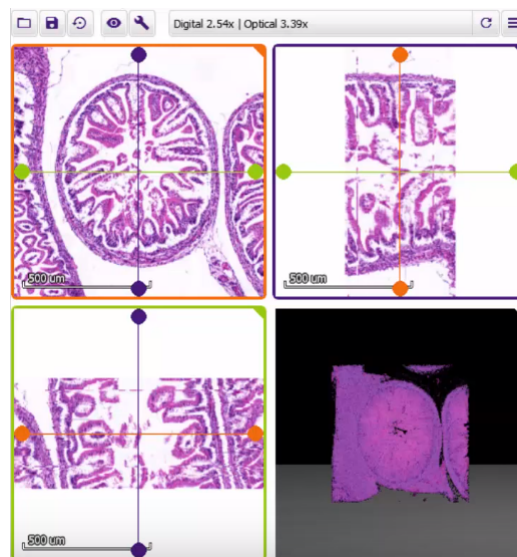
Figure 3.1: Example of a 3D reconstruction using Voloom [8].

tissue segmentation of an heart and 3D reconstruction using Mimics. The 2D images are a result of a CT scan.
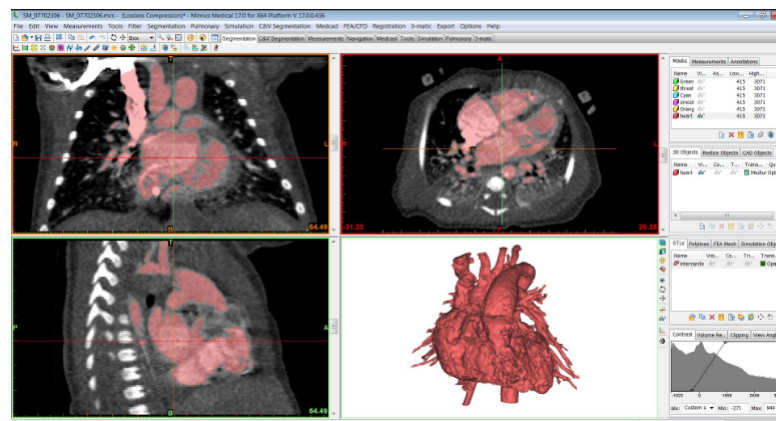
Figure 3.2: Example of a 3D reconstruction using Mimics [9].

3.2 Tissue Segmentation

Tissue segmentation consists on dividing the obtained 3D tissue structure into its constituent regions, depending on the problem. Tissue segmentation stops, ideally, when the region of interest is totally isolated. Segmentation of non-trivial images is one of the more difficult tasks of image analysis.

As referred on the previous section, Mimics is the used software for the 3D reconstruction and is also going to be used for the tissue segmentation. There are several available options for this task, including: thresholding or region grow [84], explained in section 4.3.2.

3.3   Quantitative analysis

Quantitative analysis has the main objective of estimate the relative percentage of tissue components that are present on the 3D reconstruction. On more time, this approach can be accomplished by using Mimics. With Mimics, it is possible to estimate the volume of each segmented tissue component, and this way, calculate that percentages.

Three dimensional estimation of tissue components can then be compared to the results obtained by the stain separation algorithms referred in 2.2, in order to conclude if there is any correlation between the results obtained in both methodologies.

There are some studies that try to find relationships between the analysis in both dimensions in several areas. One of them compares the performance of 2D and 3D quantitative coronary angiography (QCA) on the prediction of functional severity in coronary bifurcation lesions [85]. QCA allows to assess the bifurcation lesions dimensions, and it is used to optimize the drug-eluting stents implementation on bifurcation lesions cases, leading to an improvement of clinical outcomes. It was shown that the anatomical parameters obtained for 3D QCA acceptable and comparable to 2D QCA. Related to breast cancer, there is also a study that compares the two dimensional region of interest method for the measurement of the apparent diffusion coefficient (ADC) with a semiautomatic three-dimensional sphere for the characterization of breast lesion on x-rays mammograms [86]. ADC is measured from diffusion-weighted magnetic resonance imaging (DW-MRI), used to show the random motion of water molecules (related to the cellular density of that tissue). Since tumors are characterized by densely packed cells with diffusion restrictions, this technique can be used for find and characterize lesions. They concluded that the ADC values obtained for the 3D sphere were also comparable to 2D regions of interest. Tecelão et al compared between the 2D and 3D circumferential strain measured with MR tagging [87]. Cardiac resynchronization therapy (CRT) is used for the treatment of heart failure (HR), and due to their high cost and complexity it is necessary to assess with accuracy which patient will benefit from it. Measurement of the mechanical dyssynchrony directly appears to be the best way to predict if the patient will show improvements after CRT. The mechanical dyssynchrony can the measured based on the circumferential strain (strain on the predominant orientation of the muscle fibers) obtained from a 2D or 3D analysis. This study showed that there are no significant differences between the values obtained from the two methods.

Another studies, go further, and try to estimate the tissue volume from 2D images. Shen et al investigated the relationship between cross-sectional volume adipose tissue (VAT) areas, in different anatomic zones, and VAT volumes [88]. This study had the ultimate goal of finding which slice has the strongest relation with the VAT volume, once VAT is usually characterized by measuring the VAT area at the L4-L5 vertebral interspace. MR images were segmented and the VAT volume was calculated through Eq. 3.1, where t is the slice thickness, h is the slice gap, N is the number of slices and A is the cross-sectional area of each slice.

$$V = (t + h) \sum_{i=1}^{N} A_i \qquad (3.1)$$

They concluded that slices 10cm and 5cm (men and women, respectively) above L4-L5 have a higher correlation with the VAT volume.

Firbank and Coulthard developed a technique to estimate the extraocular volume from 2D MR images of the coronal plane [89]. Measurements of the extraocular muscle can be useful to evaluate the treatment options on thyroid-associated ophthalmopathy. After the segmentation of the extraocular muscle of each image slice, it was estimated its cross-sectional area. The volume of the muscle was computed using Eq. 3.2, where S_T is the slice thickness, S_G is the spacing between slices, N is the number of slices and A_n the area of slice n.

$$V = S_T \sum_{n=1}^{N} A_n + S_G \sum_{n=1}^{N-1} \frac{A_n + A_{n+1}}{2} \tag{3.2}$$

This method was tested in computed-generated virtual images with known extraocular muscle volumes and showed 7,6% of accuracy.

Chapter 4

Materials and Methods

In this chapter, it will be discussed the adopted methodologies and algorithms associated with the 2D histological image analysis and the tissue reconstruction, from the scanning of the slides to the reconstruction of the 3D structure of the tissue.

4.1 Tissue Samples

Images from slices of formalin-fixed paraffin embedded tissue sections were used throughout all the 2D analysis and, consequently, the 3D reconstruction. Those tissue sections were from proximal and distal vaginal tissue of sheep and were stained with Miller's Elastic Staining. Six samples of vaginal tissue (3 distal and 3 proximal) were used in this work. Each tissue was subjected to a microtome into order to cut in slices with a 6μm thickness, spaced 12μm. Each slice was placed into a slide, and contains one sample of distal tissue and one sample of proximal tissue.

4.2 Scanning of the Slides

The scanning of the slides was performed using OPTISCAN10 from OPTIKA [90]. This scanner has a resolution of 10000dpi. The parameters for the scanning were adjusted using the SciView software (interface for OPTISCAN). It was scanned a total of 2 sets of 23 slides and 1 set of 18 slides of vaginal tissues stained with Miller's Elastica Staining.

4.3 Two Dimensional Analysis

The methods comprised on the 2D analysis includes algorithms for image alignment, image segmentation and conversion to DICOM format, in order to allow the importation of the images on Mimics software, referred further ahead. The algorithms described in the section were developed using MATLAB.
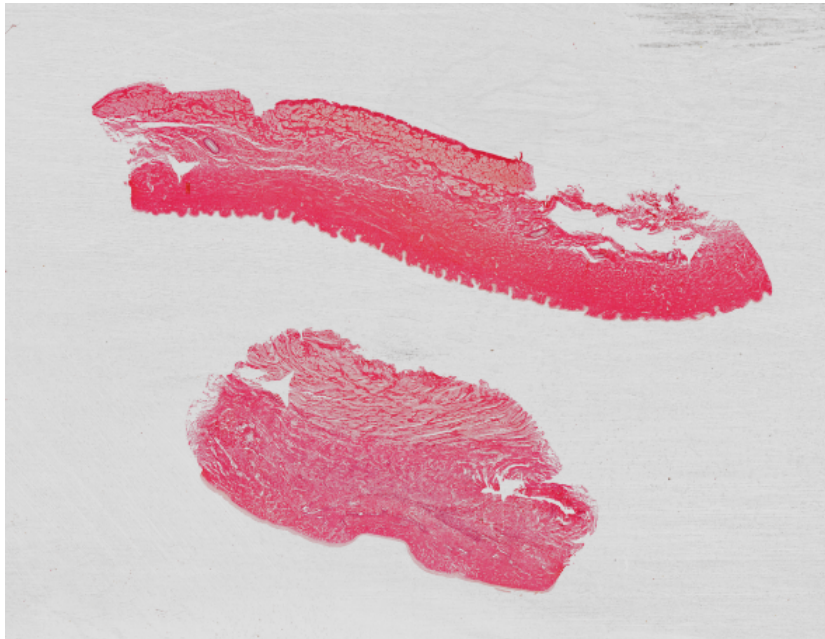
Figure 4.1: Example of an image that results from the scanning of one slide.

4.3.1   Image Alignment Algorithm

As it was mentioned on section 4.1, each slide contains 2 different types of vaginal tissues (distal tissue and proximal tissue). Therefore, the histological images that result from the scanning phase have those 2 types of tissues. Figure 4.1 shows an example of this situation. In order to align them, in the most perfect way, the original image must be cut to separate the distal from the proximal tissues.

For this purpose, it was created a small algorithm to automatically separate those tissues. For each image, a mask of the tissues was obtained using a threshold, based on the Otsu's method. After this mask is computed, the largest area (proximal tissue) and the second largest area (distal tissue) are selected, and their extreme coordinates (top, bottom, left and right) are determined. Those coordinates are, then, used to cut, automatically, the original image in order to get the smallest possible images with the isolated tissues. At the end of this part, each previous set of images was split in 2 sets of smaller images with the distal and the proximal tissues.

Once this problem was solved, an algorithm for the alignment of each set of images was developed. The pseudocode for this algorithm is shown in Algorithm 1.

The image alignment algorithm starts by reading 2 consecutive images of one set. The first image that is read is the reference image and the second is the sensed image. The reference image is considered as already aligned. Both images are binarized using an automated threshold, based on the Otsu's method. Then, centroids of 2 regions of interest (ROI) per image are computed. Those centroids will be used as points by which the alignment will be done. The ROIs are selected manually by the user around the area highlighted in Fig. 4.2. These areas result from a needle that was used prior to the fixation of the tissue on paraffin, in order to have a guide to perform the

---

Algorithm 1 Image Alignment

 1: **for** j = 1 to number of images **do**
 2:     **for** i = 1 to 2 **do**
 3:
 4:         *Read image*
 5:         *Binarize image*
 6:         *Select 2 ROI*
 7:         *Apply Canny to the ROI*
 8:         *Morphological operations to the ROI*
 9:         *Determine the centroid of each ROI*
10:
11:     **end for**
12:     *Translation of the sensed image to overlap the right centroid of the reference image*
13:     *Update the centroid coordinates of the sensed image*
14:     *Set the coordinates of the overlapped centroids as the rotation point*
15:
16:     **if** ordinate(centroid2 of image1) < ordinate(rotationPoint) AND
17: ordinate(centroid2 of image2) < ordinate(rotationPoint) **then**
18:         **if** *ordinate(centroid2 of image1) < ordinate(centroid2 of image2)* **then**
19:             $\alpha = -(\theta - \beta)$
20:         **else if** *ordinate(centroid 2 of image2) < ordinate(centroid 2 of image1)* **then**
21:             $\alpha = \beta - \theta$
22:         **end if**
23:     **end if**
24:
25:     **if** ordinate(centroid2 of image1) > ordinate(rotationPoint) AND
26: ordinate(centroid2 of image2) > ordinate(rotationPoint) **then**
27:         **if** *ordinate(centroid2 of image1) < ordinate(centroid2 of image2)* **then**
28:             $\alpha = -(\beta - \theta)$
29:         **else if** *ordinate(centroid 2 of image2) < ordinate(centroid 2 of image1)* **then**
30:             $\alpha = \theta - \beta$
31:         **end if**
32:     **end if**
33:
34:     **if** ordinate(centroid2 of image1) > ordinate(rotationPoint) AND
35: ordinate(centroid2 of image2) < ordinate(rotationPoint) **then**
36:         $\alpha = \beta + \theta$
37:     **end if**
38:
39:     **if** ordinate(centroid2 of image1) < ordinate(rotationPoint) AND
40: ordinate(centroid2 of image2) > ordinate(rotationPoint) **then**
41:         $\alpha = -(\beta + \theta)$
42:     **end if**
43:
44:     *Rotate image2 by α*
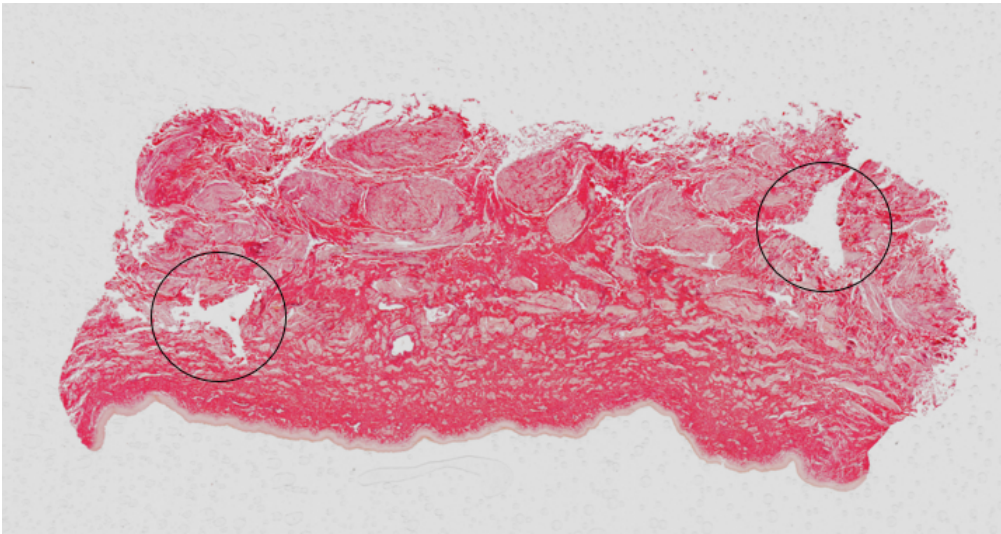45:   *Save image*
46: **end for**

Figure 4.2: Example of an histological image of distal tissue. The highlighted areas show the desired location of the ROIs that are selected by the user.

three dimensional reconstruction. The selected ROIs were subjected to a post-processing phase that allowed to obtain its edges. The Canny edge detector was used for the edge detection of the ROIs, and morphological operations, such as the image closing, was used to close the obtained edges. As soon as the edges were determined, its centers (centroids) were computed. Thus, each sensed image will be associated to 2 centroids that, ideally, should overlap the other 2 centroids of the reference image.

Having the centroids calculated, two translations followed by a rotation were performed to the sensed image to align it with the reference image. Thereby, the sensed image is, then, translated in a way that allows the overlapping of the right centroids of both images. Next, the right centroid (already overlapped with the reference image and, therefore, with the same coordinates) is considered the rotation point for the rotation that will enable the image alignment. This rotation may not cause the overlapping of the left centroids due to distortions upon the slicing of the tissue with the microtome. So, this rotation will only ensure that the left centroids of both images are in the same direction. The angle (α), by which the second image has to rotate, was computed using trigonometry. The different conditions present on Algorithm 1 are related to the different positions of the left centroids of both images when compared to the rotation point, as shown in Fig. 4.3.

Once all images of one set are aligned, another small algorithm was developed to automatically adjust the size of each aligned image, so that every image of a set have the same size. This way, it was computed the size of the largest image of the set, and then, added, to each image, black pixels to the right and bottom borders. Adding pixels to these borders do not affect the alignment.

4.3.2   Image Segmentation

The image segmentation phase has the objective of segment the elastin and collagen present on each slice. To accomplish this segmentation, it was fisrt used the Color Deconvolution algorithm
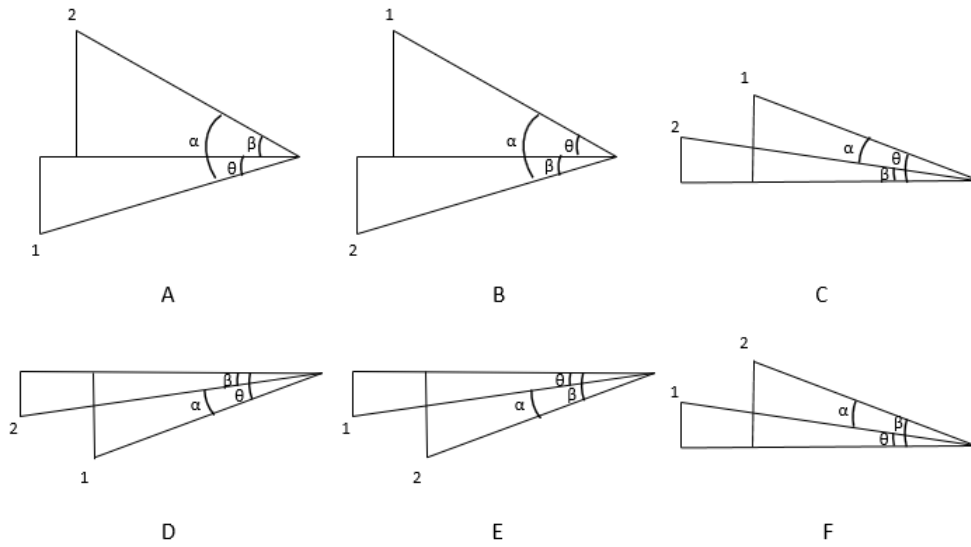
Figure 4.3: Auxiliary images used to calculate the angle of rotation (α) that allows the alignment of two images. Points 1 and 2 are the left centroids of the reference and sensed images, respectively.

based on [57], as mentioned on section 2.2.1.1. Algorithm 2 contains the pseudocode for the used Color Deconvolution algorithm.

Algorithm 2 Color Deconvolution

 1: *Definition of the OD matrix*
 2: *Normalization of the OD matrix*
 3: *Computation the inverse of the normalized OD matrix*
 4: *Computation the optical density of the image*
 5: *Reshape each channel to one column*
 6: *Multiplication the reshaped image for the inverse of the OD matrix*
 7: *Reshape the result for the original size of the image*
 8: *Normalization of the image*

The developed Color Deconvolution algorithm starts by defining the optical density matrix, similar to the matrix referred in Eq. 2.7. The values of this matrix depend on the colors that are going to be separated. This matrix is normalized by dividing each value by the length of the corresponding stain vector (line of the matrix) and, then, the result is inverted. The optical density for the image was calculated based on Eq. 2.6. The product of the optical density of the input image and the optical density matrix gives a RGB image, where each channel contains the information for the correspondent color of the stain vectors used to define the OD matrix. This RGB image was normalized by applying Eq. 4.1 to each one of the 3 channels. Any channel of the output image contains a gray-level image, thus the maximum and minimum possible values for its pixels are 255 and 0, respectively, as present in Eq. 4.1.

$$imageChannel = \frac{(imageChannel - min(imageChannel)) \times (255 - 0)}{(max(imageChannel) - min(imageChannel)) + 0} \tag{4.1}$$

The first channel of the output image is associated with collagen and the last with elastin. As they contain gray-level images, the whiter pixels are the pixels that should be segmented in order to obtain those tissue components.

Having this in mind, the next goal is to segment those pixels for the first and last channels, to obtain the total content of collagen and elastin for each slice. The next two sections will focus on the processes for the segmentation of this two tissue components.

4.3.2.1 Collagen Segmentation

As mentioned before, the goal is to segment the whiter pixels, in this case, of the first channel of the obtained RGB image. The main idea of the algorithm is to find a threshold that better segments these pixels of the image.

Figure 4.4 shows the RGB image that is going to be used to illustrate how this algorithm works. After applying the color deconvolution algorithm, to the image present in Fig. 4.4, and selecting the first channel, it was obtained the image from Fig. 4.5. In Fig. 4.6, there is the histogram for the image present in Fig. 4.5. Collagen pixels are located in the second half of the last peak of the histogram. This area was determined based on the observation of several histograms of images after the color deconvolution algorithm.

Applying the Otsu's method directly to the image caused the segmentation of some light red pixels that did not correspond to collagen areas. Instead, it was used the Otsu's method to first segment the last peak of the histogram. The value for the obtained threshold was used to perform a contrast adjustment operation, turning into 0 every pixel bellow that value. This operation led to a better separation of the gray tones of the image and the result is shown in Fig. 4.7. A second Otsu's method was applied to this image to segment collagen.

At the end, the binary image with the segmented collagen was multiplied by a mask of the tissue, to assure that the segmented collagen just derives from a part of the image that contains tissue. This final step is important due to the presence of some artifacts in the original images. In case the image do not have non-tissue zones, this step is not occur.

4.3.2.2 Elastin Segmentation

The elastin segmentation is accomplished using the third channel of the RGB image that results from the color deconvolution algorithm. In a similar way to the collagen segmentation, the goal is to determine the threshold that segments the whiter pixels of the image.

In order to determine the best value for the threshold, it was computed the histogram of the image, as shown in Fig. 4.8. The elastin is located at the end of the histogram, starting in the position where the histogram begins to decrease slower. To find this position, it was calculated
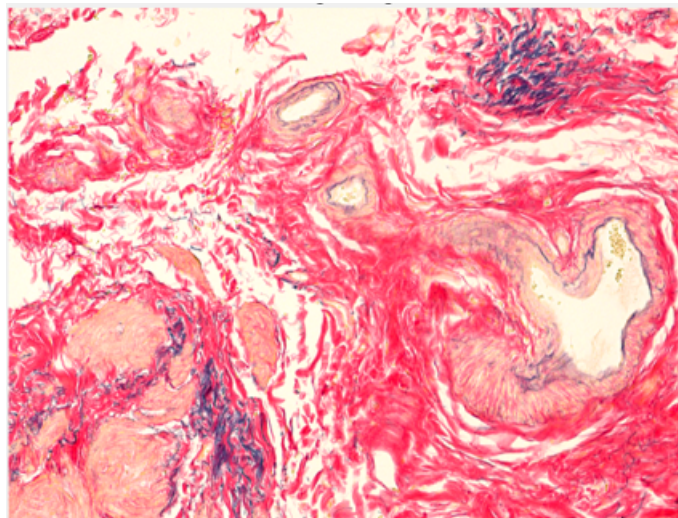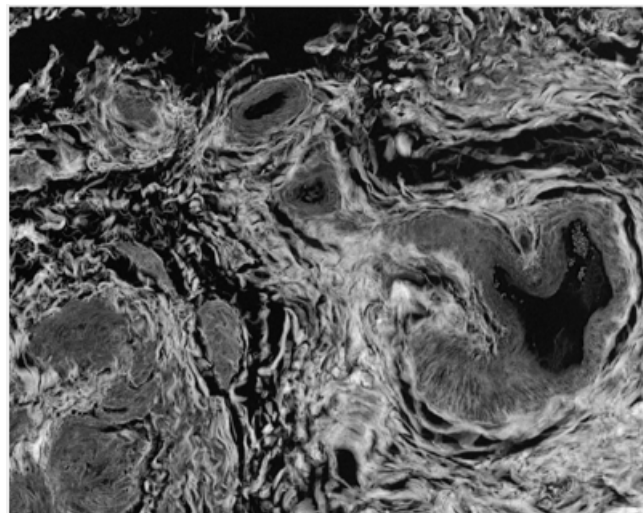
Figure 4.4: Original RGB image.

Figure 4.5: Gray-level image obtained from the first channel of the RGB image that results from the color deconvolution algorithm applied to Fig. 4.4. The whiter pixels of this image corresponds to the pixels for collagen.
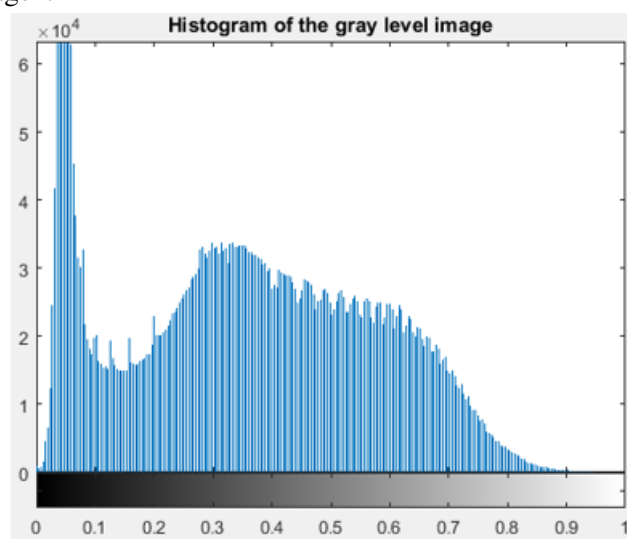
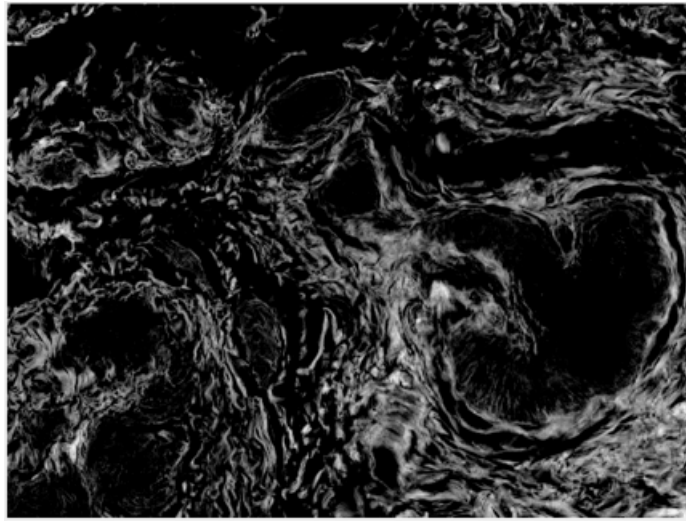

Figure 4.6: Histogram for Fig. 4.5.

Figure 4.7: Gray-level image after the contrast adjustment.

the gradient of the histogram (first derivative) and the absolute value of this gradient, as present in Figs. 4.9 and 4.10. When the histogram begins to decrease slower, the gradient, and consequently, its absolute value, reaches values close to 0. So, considering the last peak of the histogram, the threshold value was set to be the value where the gradient decreases to 5% of its maximum.

Once the threshold is determined, the image is binarized and multiplied by a mask of the tissue. One more time, if the image do not contain any background zones, this part of the algorithm is not used.

4.3.3   Percentages of Elastin and Collagen

For the computation of the percentages of elastin and collagen, it was created a binary mask of the whole tissue that is present in each image. The area of this mask was calculated and considered as the total area of the tissue. The obtained binary images for the collagen and elastin were also read and its areas were determined. Based on these information, the percentages for each type of tissue component were obtained.

4.3.4   Conversion to DICOM

The binary images of elastin and collagen had to be converted to DICOM, in order to allow their importation to Mimics. The conversion to DICOM was done directly with MATLAB, but the metadata associated with each DICOM image was created manually. The information that was modified/created on the DICOM metadata file was:

- **Slice Thickness** - Thickness of each slice in mm.

- **Pixel Spacing** - Physical distance between the center points of each pixel (x and y) in mm.

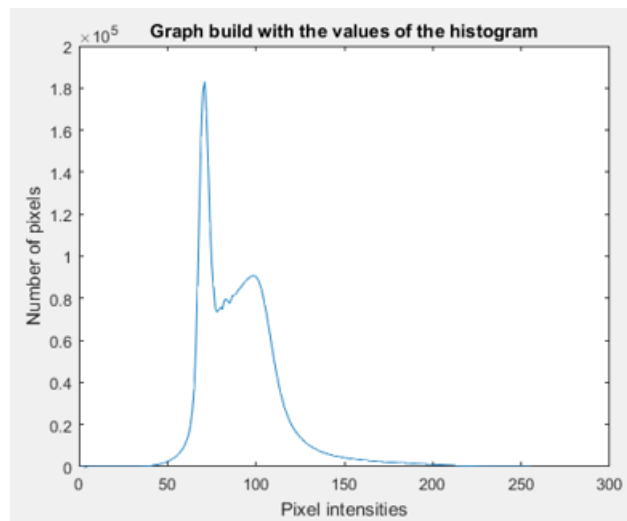- **Instance Number** - Number that identifies the image.

Figure 4.8: Example of an histogram of the last channel of the RGB image that results from the color deconvolution algorithm.
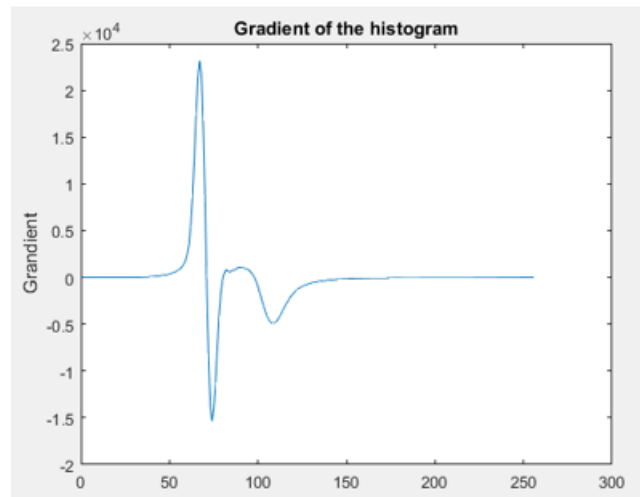

Figure 4.9: Gradient for the histogram present in Fig. 4.8.
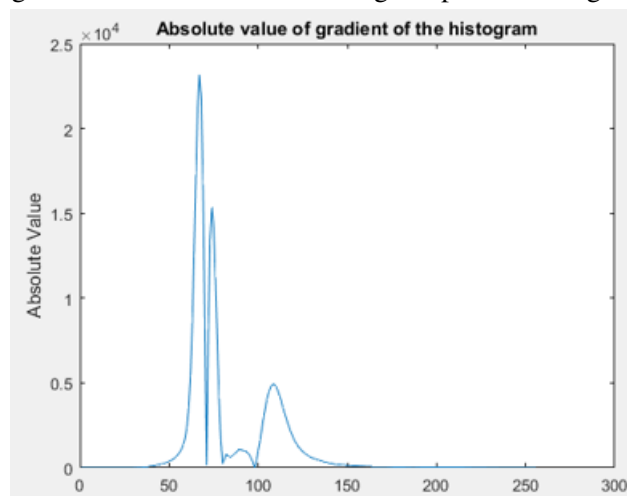
Figure 4.10: Absolute value of the gradient for the histogram present in Fig. 4.8.

- **Slice Location** - Location of each slice, in the z axis.

- **Spacing Between Slices** - Distance between consecutive slices.

- **Study Description** - Name that identifies the study.

- **Series Description** - Name that identifies the series.

In order to determine the pixel spacing attribute, it was scanned a sheet of millimeter paper and, based on the image size, it was determine the distance between pixels centers.

The metadata file contains other attributes that are automatically created upon the conversion to DICOM, however the attributes that were referred previously are the important parameters for the configuration of the 3D reconstruction.

4.4   Three Dimensional Reconstruction

The three dimensional reconstruction was accomplished using the software Mimics. The DICOM images obtain through the methodology previously described were imported to Mimics to reconstruct the tissue. It was defined a mask to segment only the binary part of the images and, finally, the tissue was reconstructed from that mask, using a custom reconstruction (based on the contour).

For this part of the work, the percentages of collagen and elastin were determined based on the volume of the reconstructed tissues.

Chapter 5

Results and Discussion

5.1 Scanning of the Slides

The scanning of the slides were done without any zoom of the slide and with a custom configuration. This configuration was set in order to obtain a good contrast between all tissue components, mainly elastin and collagen, and to keep the yellowish tone present in the histologies. It was chosen the value of -15 for saturation and 15 for brightness. In Fig. 5.1, there is an example of an image that results from the scanning of one slide. Each image had the size of 14368x9572 pixels.

5.2 Two Dimensional Analysis

5.2.1 Image Alignment

The separation of the proximal and the distal tissues, before the alignment algorithm, was an essential step for the success in the image alignment phase. Having both tissues on the same image compromised the correct alignment of both proximal and distal tissues. When the distal tissue, of two consecutive images, was aligned, the proximal tissue was misaligned and vice versa. Cutting the original images was also a very important step to reduce their size and, consequently, the computational cost of the algorithms applied after the alignment. The result of this small algorithm, applied to the image present in Fig. 5.1, is shown in Fig. 5.2. As it can be seen, the algorithm successfully separated the tissues. However, if one of the tissues, from a given image, is cut, the algorithm will only select the two largest areas. In this case, this separation has to be done manually or a portion of tissue is going to be eliminated. Figure 5.3 shows an example of this situation. The smaller portion, of the distal tissue, will not be present on the image that is going to be formed.

Concerning the alignment algorithm, the centroids computation is the key factor for a favorable outcome. If the centroids are determined successfully, all images are going to be aligned by the same points, and the results will be more accurate. In Fig. 5.4, there is an example of the determination of the two centroids for one of the images. Centroids are represented by red circles. As it can be seen from this image, centroids were calculated perfectly with the developed algorithm.

35

Figure 5.1: Image that results from the scanning of one slide (original scan).
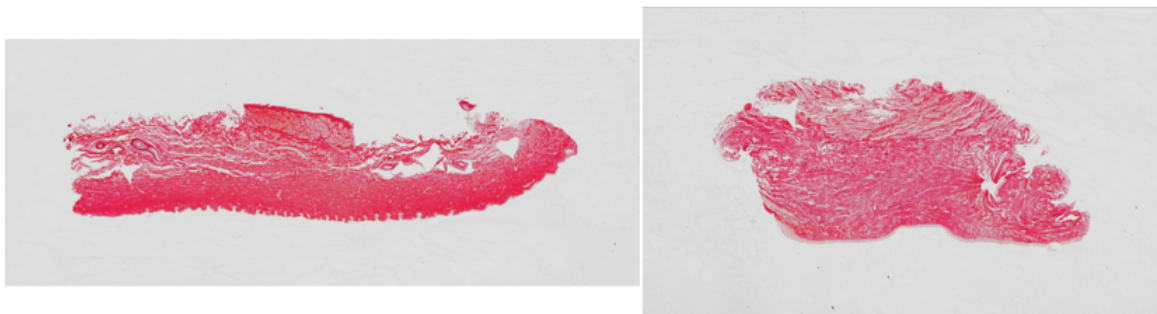
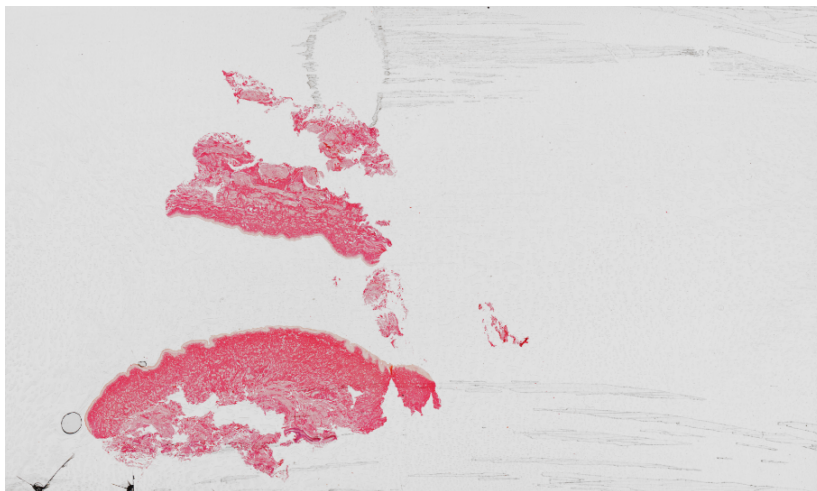

Figure 5.2: Images with the isolated tissues.

Figure 5.3: Image that illustrates the situation where the algorithm, to automatically cut the images, do not give satisfactory results.
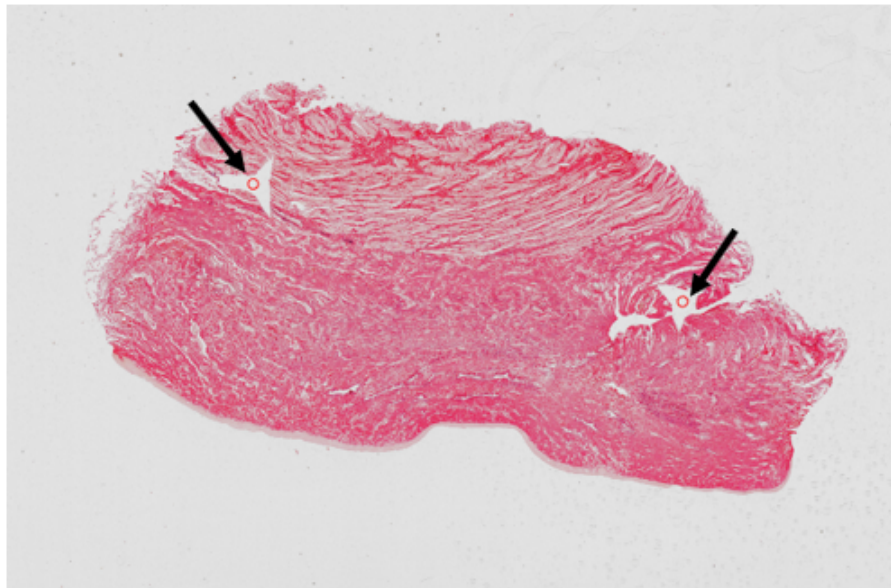
Figure 5.4: Results for the determination of the centroids for one image.

Images where there is a lot of inaccuracy upon the selecting of the ROIs by the user, can lead to some errors in the alignment, since centroids decide the translations and rotations that will occur to the sensed image. Figure 5.5 shows an example of one image of distal tissue, where it is almost impossible to select, accurately, the ROIs for the centroids determination. The right centroid do not have a well defined area for the selection of its ROI.

A rigid transformation, to align the sensed image with respect to the reference image, was applied after the centroids determination, and the result, for two of the images, is shown in Fig. 5.6. In purple is the reference image and in green the image that was aligned. As shown in Fig. 5.6, the ROI of the right side is perfectly overlapped with the first image, while the ROI of the left side do not verify the same situation, as expected. An overlapping of the centroids lead to an overlapping of the ROIs. As explained in the previous chapter, the overlapping of the left centroids may not happen, because it is only assured that the direction of both centroids is the same. Left centroids do not perfectly overlap, mainly, due to some tissue distortions caused during the slicing. Besides, there is also the spacing between slices factor, which is twice the slice thickness. There may be some differences in the next slice with respect to the previous slice, due to their the distance on the tissue. If the overlapping of both left and right centroids were required, instead of just applying translations and rotations to the sensed image, scaling transformations also had to occur. Scaling of the images is an unwanted transformation once it changes the original scale of the images.

Despite all this, in almost every cases, the alignment was accomplished with success and these factors did not had a large influence in the images, as can be seen in Fig. 5.7. However, even if the alignment is successful, there are parts of the tissues that, sometimes, are distorted or cut, affecting the overall alignment.

To avoid the the cases where the misalignment would be certain, not all the images of each set

Figure 5.5: Image the distal tissue, where it is difficult to select the best ROI for the determination of the centroids position.

were used on the alignment and, consequently, on the 3D reconstruction because the first slices did not contain much tissue (Fig. 5.8C), other slices had some tissues cut (Fig. 5.8B), or the ROI for the centroids were impossible to determine accurately (Fig. 5.8A).

After selecting and aligning all sets of scanned images, it was obtained a set with 21 images, 2 sets with 15 images, 1 set with 11 images and 2 sets with 10 images.

5.2.2   Image Segmentation

Although the segmentation of collagen and elastin was performed using MATLAB, there was also the possibility of importing all images of a set to Mimics, and perform, there, this segmentation. This hypothesis was dismissed because of the images size and, most importantly, the fact that Mimics do not allow the importation of RGB images. The initial RGB images would have to be converted to gray-level images, which would remove the color information that is important for the segmentation. Figure 5.9 shows the gray level image for Fig. 5.2. Analyzing this image, it is possible to see that the initial bluish (elastin) and reddish (collagen) tones are converted to approximately the same gray-level values, making it more difficult separate the different components. Even if Mimics allowed the use of RGB images, it would be hard to manipulate them. Images, used in this work, have higher resolution than medical images, which requires a lot of resources, making this a very time consuming task. In addiction, the threshold values for the segmentation would have to be defined by the user, leading to subjective results. Having this in mind, it was decided to perform the segmentation of elastin and collagen prior to the importation to Mimics.

The color deconvolution algorithm was the chosen algorithm for the separation of the different colors present on each slice. Since collagen acquires a reddish color and elastin a bluish color, the
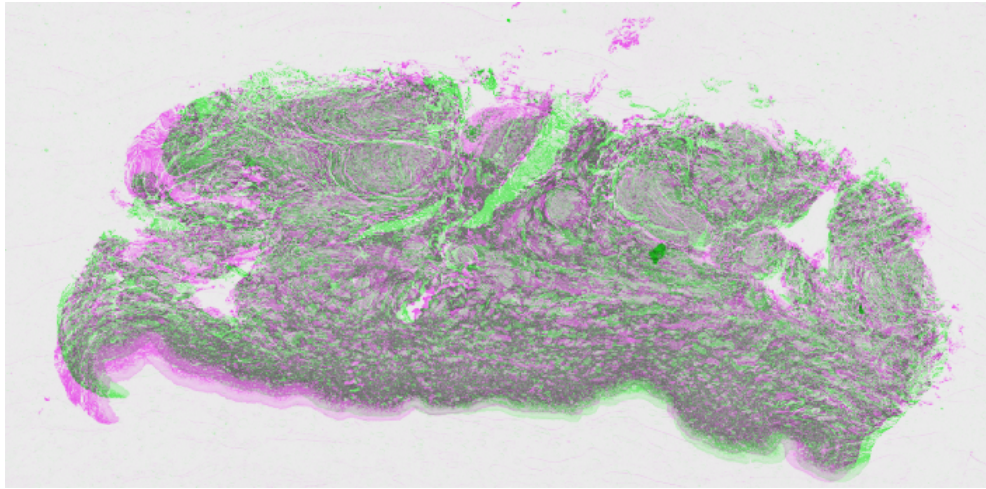
Figure 5.6: Result for the alignment of two images of distal tissue. The left ROI is not overlapped with the reference image.
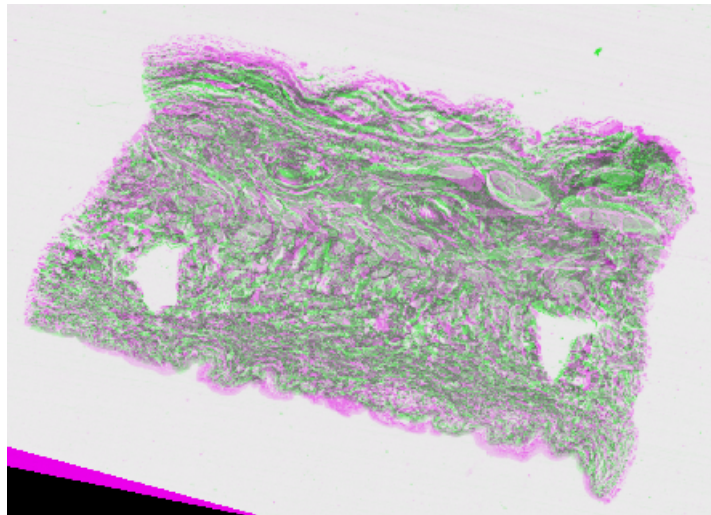

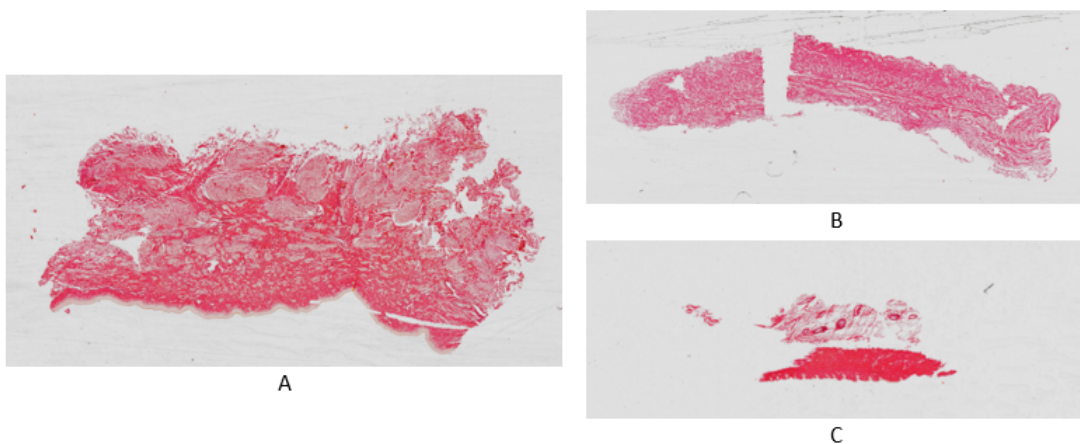Figure 5.7: Result for the alignment of two images of distal tissue.

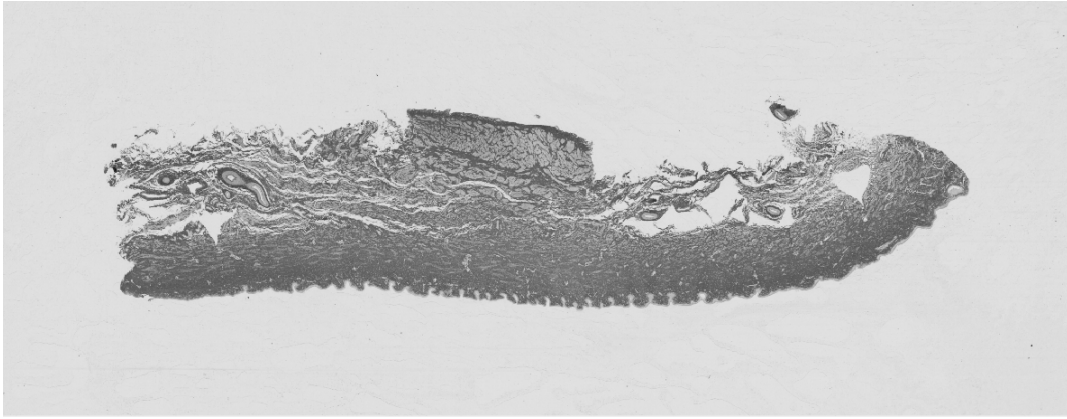Figure 5.8: Examples of malformations of some slices.

Figure 5.9: Gray-level image for the image present in Fig. 5.2

used optical density matrix, shown in Eq. 5.1, was based on the RGB vectors.

$$\begin{bmatrix} 0 & 1 & 1 \\ 1 & 0 & 1 \\ 1 & 1 & 0 \end{bmatrix} \tag{5.1}$$

As referred in the previous chapter, the result of the color deconvolution algorithm is a RGB image, where, in this case, the first channel corresponds to the gray-level image that contains the information about collagen, and the last channel the image that contains the information about elastin. In Fig. 5.10 is the gray-level image for collagen and in Fig. 5.11 is the gray-level image for elastin, both as a result of the developed color deconvolution algorithm. Figure 5.12, on the other hand, is the original image used as input for the algorithm.

The whiter pixels of Figs. 5.10 and 5.11 correspond to the areas where collagen and elastin are located and, therefore, the areas that are going to be segmented. Comparing those images with Fig. 5.12, it is possible to see a match between the reddish and bluish zones with the whiter areas of Figs. 5.10 and 5.11, respectively.

Since this is a stain separation algorithm, changes in the illumination of the images will cause problems on the separation of the desired colors. In this case, it was used a scanner, so the illumination was uniform. When it is used a microscope, the illumination of the captured images will be influenced by the illumination of the microscope itself and by the illumination of the surrounding area, which can lead to some errors when using this kind of algorithms. It would be better if, in this situations, it is used an algorithm to remove the uneven illumination before the stain separation algorithms.

The gray-level images, that result from the color deconvolution algorithm, are used as input to a segmentation algorithms, in order to segment collagen and elastin. Figures 5.13 and 5.14 contain the results of the segmentation algorithms described on section 4.3.2 for collagen and elastin, respectively. Comparing Figs. 5.10 and 5.13 and Figs. 5.11 and 5.14 it is possible to conclude that, visually, the whiter pixels of both images were segmented.

Figure 5.10: Result for the first channel (collagen) of the RGB image obtained from the color deconvolution algorithm.
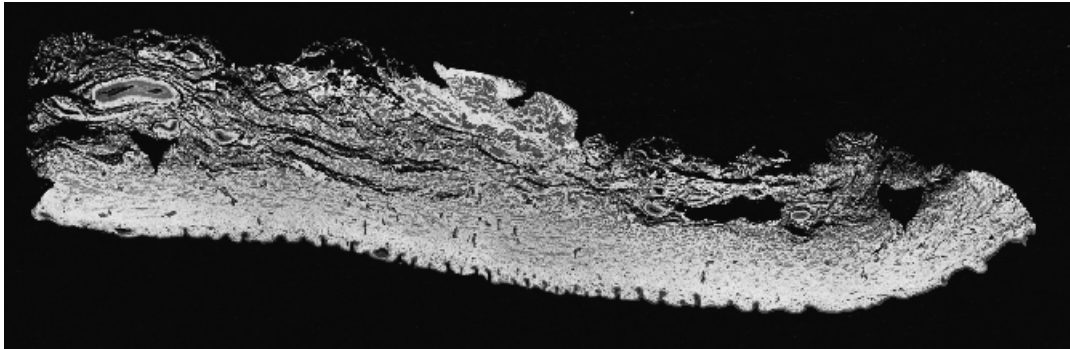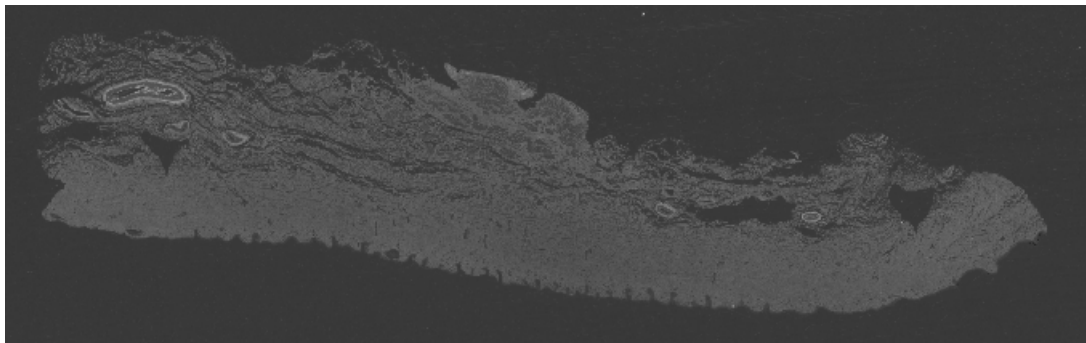

Figure 5.11: Result for the last channel (elastin) of the RGB image obtained from the color deconvolution algorithm.
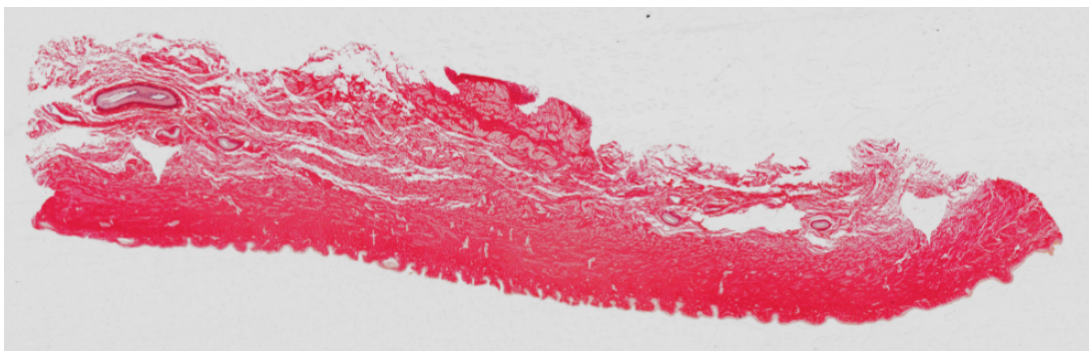

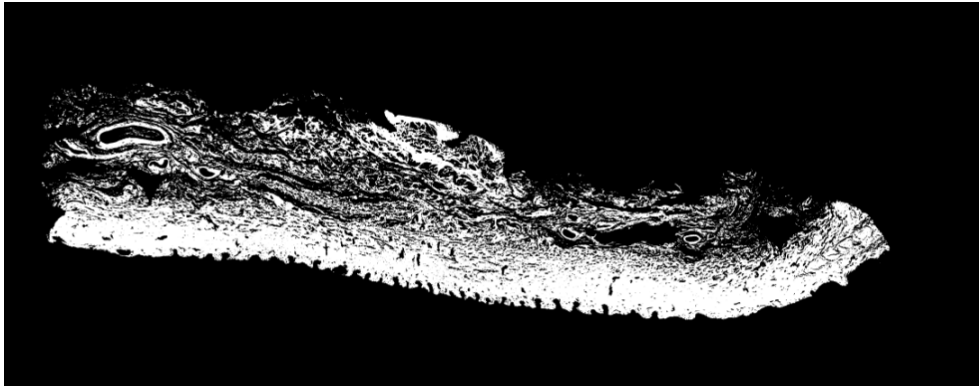Figure 5.12: Original image.

Figure 5.13: Result for the collagen segmentation performed in the image present in Fig 5.10.
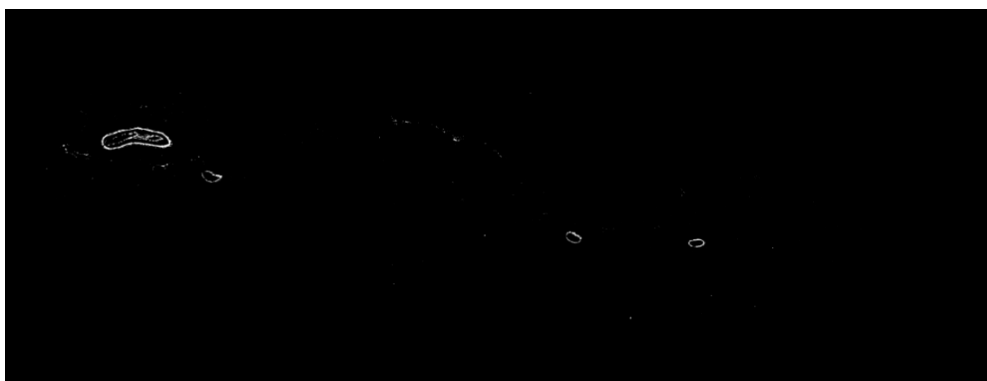

Figure 5.14: Result for the elastin segmentation performed in the image present in Fig. 5.11.

Table 5.1: Results of the robustness tests for the segmentation algorithm.

	Percentage of Elastin	Percentage of Collagen
1 st Test	0.32	60.33
2 nd Test	0.32	60.36
3 rd Test	0.32	60.36
Average	**0.32**	**60.35**
Standard Deviation	**±0.00**	**±0.01**

Before assessing the results of the segmentation algorithms, it was important to conclude about its robustness. If an algorithm is robust, it will give the same results if the input image is the same. This way, it was chosen a set of 15 images and its segmentation was done three different times, using the algorithms describes in the previous chapter. With the obtained binary images, it was computed the percentages of elastin and collagen of each slice of the set, and the results of the segmentation algorithm were compared using these percentages. The results for these tests are shown in Table 5.1 and represent the average percentage of each component on the set of images. As it can be seen in Table 5.1, the algorithm originated the same percentages of elastin and collagen for the 3 tests. So, it is safe to consider that the developed algorithm is robust.

Once the robustness of the algorithm have been proven, it was also interesting to compare the results of the automatic segmentation to the results of a manual segmentation. The manual segmentation of the images was accomplished using ImageJ [91], an open source image processing program. ImageJ was the chosen software for the manual segmentation, because there is literature that already showed that the results obtained with ImageJ, for collagen segmentation, are comparable with the results obtained with the gold standard hydroxyproline assay [24]. As also described in [24], images are subject to a color deconvolution plug-in, in ImageJ, to separate the different stains, similar to what was done automatically. After, it is adjusted, manually, a threshold to segment the components, and the percentages were computed.

For this task, it was used 3 different images captured by a microscope, instead of the digitized images that were used for the development of the algorithms. These images were carefully chosen, in order to avoid situations where there was non-uniform illumination. Then, a group of 10 people, from different backgrounds, followed this methodology to obtain the percentages of collagen and elastin for the manual segmentation. Those chosen images are simpler to understand and segment by people who do not have a biology background. Figure 5.15 shows an example of an image that was used for this purpose. Using different images will also prove that the developed algorithm is robust enough to deal with images from different sources.

Table 5.2 shows the results for the manual and automatic segmentation for each of the 3 images. For the manual segmentation, the results correspond to the average percentage calculated from the 10 different segmentation. As the developed algorithm is robust, it was only performed one automatic segmentation. As it can be seen from Table 5.2, both the results for manual segmentation and automatic segmentation are similar, but the standard deviation is close to 1% in some cases.
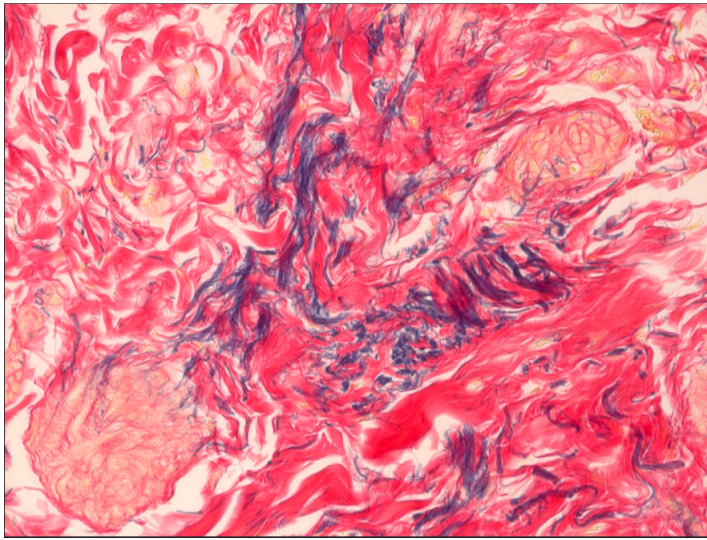
Figure 5.15: One of the images used to perform the manual segmentation.

In order to see how the results for the segmentations are distributed for each image, it was created the box plots shown in Figs. 5.16, 5.17 and 5.18. The whiskers of the box plots indicate the obtained maximum and minimum percentages for each case. In general, all of the obtained box plots were long, which means that the percentages for the manual segmentation of elastin and collagen were dispersed. This also explains why the standard deviation was close to 1%. The median of the manual segmentation was similar to the median of the automatic segmentation, most of the cases. This can be explained by the fact that the 10 people performing the manual segmentation are from different backgrounds and, this way, not very familiar with histological image analysis. This manual segmentation is also subjective and depends on what each user considers elastin and collagen.

It was, as well, performed pared t-tests to compare the results for the manual and automatic segmentation for each image. The results for the elastin segmentations were p=0.106, p=0.454 and p=0.584, and the results for the collagen segmentation were p=0.339, p=0.001 and p=0.600, for the first, second and third images, respectively. The segmentation of collagen, for the second image, was the only case were the results were statistically different (p=0.001). All the other results were higher than 0.05 and, therefore, not statistically different.

Table 5.2: Comparison between manual segmentation and automatic segmentation. The results for the manual segmentation are expressed as the average percentage of elastin and collagen performed by 10 people.

	Elastin (Automatic)	Elastin (Manual)	Collagen (Automatic)	Collagen (Manual)
Image 1	4.22	4.06±0.29	24.55	24.85±0.92
Image 2	10.22	10.43±0.80	46.99	45.83±0.70
Image 3	15.22	15.33±0.63	28.20	28.31±0.66
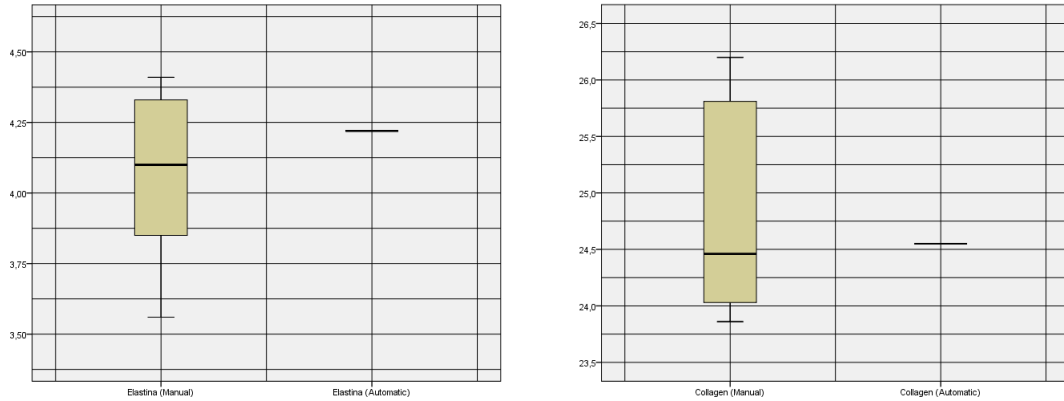
(a) Distribution of the percentages of elastin in the manual and automatic segmentation for the first image.

(b) Distribution of the percentages of collagen in the manual and automatic segmentation for the first image.

Figure 5.16: Box plots for the manual and automatic segmentation of the first image.
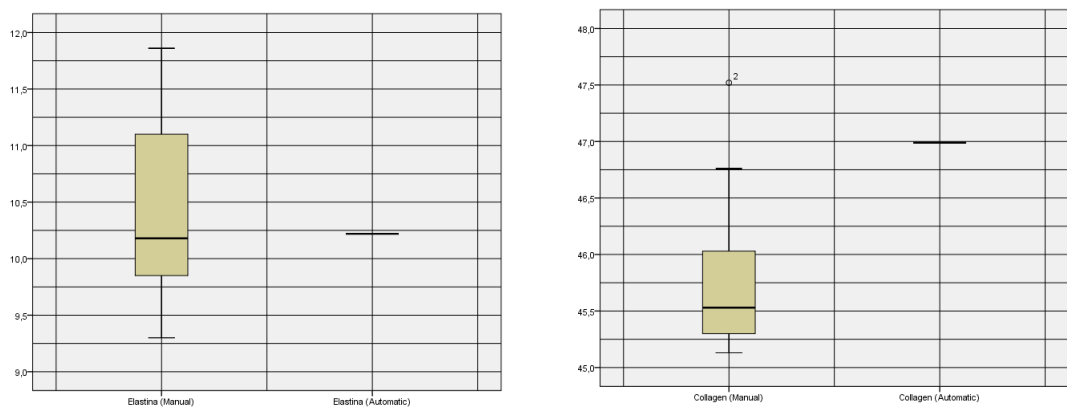
(a) Distribution of the percentages of elastin in the manual and automatic segmentation for the second image.

(b) Distribution of the percentages of collagen in the manual and automatic segmentation for the second image.

Figure 5.17: Box plots for the manual and automatic segmentation of the second image.
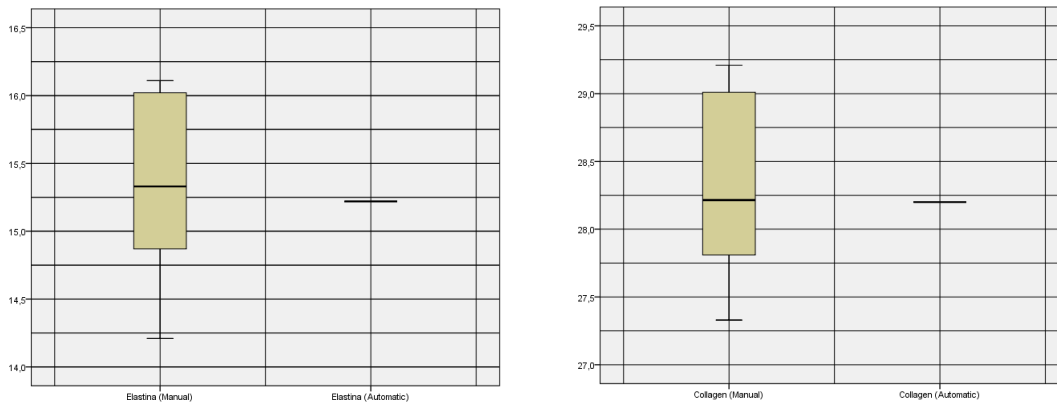
(a) Distribution of the percentages of elastin in the manual and automatic segmentation for the third image.

(b) Distribution of the percentages of collagen in the manual and automatic segmentation for the third image.

Figure 5.18: Box plots for the manual and automatic segmentation of the third image.

Considering all of this information, it is possible to see that the developed algorithm produce results that are comparable to the results obtained from a manual segmentation using ImageJ.

5.3   Three Dimensional Reconstruction

Binary images, that result from the segmentation algorithm, were converted to DICOM and imported to Mimics to obtain the 3D reconstruction of elastin and collagen. In Fig. 5.19, there is an example of the reconstruction obtained for elastin for one of the sets of images. As it can be seen by this figure, the reconstruction was very coarse, which can be explained by the fact that the distance between slices is twice the slice thickness. With the spacing between slices that large, there is a need for a lot of extrapolation of the possible missing tissue. Although the distance between slices and slice thickness are very small (0,012mm and 0,006mm, respectively), at the scale of the tissue structures, this small distances are significant.

Through an observation of several elastin reconstructions, it was also possible to see that Mimics can not reconstruct consecutive slices if the same information is distant in x and y. If two consecutive slices contained information at, approximately, the same x and y positions the reconstruction occurred, but if the same structure occupied distant x and y positions the reconstruction is not successful. There is also the problem associated with the fact that, during the slicing, the tissue suffers some distortions that affect the perfect alignment of the images. Consequently, this slightly misalignment interfere with the distance, in x and y, of the information that is present in each slice, leading to errors during the reconstruction. The used distance between slices can also interfere with these distances em x and y.

Figure 5.20 shows a section of the 3D reconstruction of collagen for one set of images. As slices with collagen contained more information, the problem related to the distance in x and y
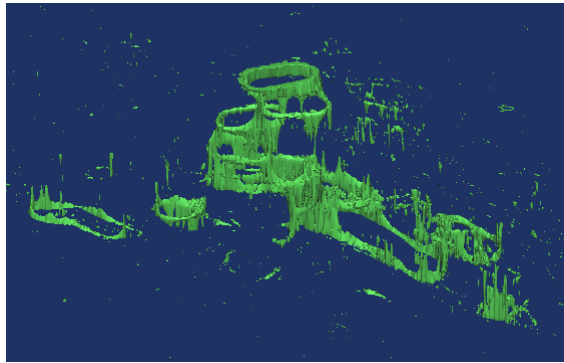
Figure 5.19: Section of the three dimensional reconstruction of elastin for one set of images.

directions had less importance. However, areas were the amount of collagen is low, showed also some problems, similar to what was described for elastin reconstruction.

Another goal of this work was to see if it is possible to compare the volumes obtained through the 3D reconstruction and the volumes estimated from the 2D images. So, after computing the three dimensional reconstruction of the tissues and its components, is was determined the corresponding volumes, in order to calculate the percentages of elastin and collagen. These volumes were given directly by Mimics. Then, using Eqs. 3.1 and 3.2, the results for the areas of each slice of elastin and collagen were used to estimate its 3D volume. These results, represented in Tables 5.3 and 5.4, were compared to the results obtained using Mimics.

Since Eq. 3.1 and Eq. 3.2 describe different things, as explained in section 3.3, it was expected that the percentages for elastin and collagen were different. Equation 3.2 seemed more accurate than Eq. 3.1, because it considers the average amount of tissue of two consecutive slices for the estimation of the spacing between slices tissue, instead of the total amount of tissue of only one of the slices. However, the results were practically the same in both cases.

Concerning the elastin reconstruction, all of the reconstructions of all of the sets showed a smaller volume, when compared to the volume estimated from the 2D images. This can be explained by the fact that Mimics was not able to successfully reconstruct the tissue. Due to the relatively high spacing between slices, the reconstruction was compromised when portions of the tissue, in two consecutive slices, were far from each other (x and y directions). Thus, there is a lack o tissue on that zone and, consequently, the obtained volume is lower than the expected. The reconstruction of collagen originated also some differences between the volumes determined by Mimics and the volumes that result from the estimation from the 2D images. Nevertheless, as the reconstructions were not accurate it is not possible to conclude about the relation between the 3D volumes and the estimations from the 2D images.
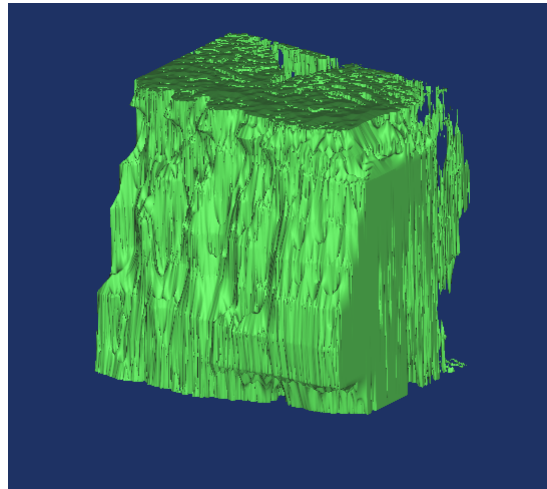
Figure 5.20: Section of the three dimensional reconstruction of collagen for one set of images.

Table 5.3: Results for the volume of elastin, in mm^3, obtained by Mimics and by Eq. 3.1 and Eq. 3.2.

	Volume - Mimics	Volume - Eq. 3.1	Volume - Eq. 3.2
Set 1	0.06	0.25	0.25
Set 2	0.12	0.31	0.31
Set 3	0.37	0.85	0.86
Set 4	0.01	0.07	0.07
Set 5	0.06	0.30	0.31
Set 6	0.17	0.45	0.46

Table 5.4: Results for the volume of collagen, in mm^3, obtained by Mimics and by Eq. 3.1 and Eq. 3.2.

	Volume - Mimics	Volume - Eq. 3.1	Volume - Eq. 3.2
Set 1	45.14	40.54	40,58
Set 2	52.11	47.52	47.83
Set 3	29.23	27.13	27.32
Set 4	36.89	36.27	36.74
Set 5	38.55	36.46	36.44
Set 6	55.50	48.54	48.63

Chapter 6

Conclusion

Histological images can provide detailed information about tissue structure and, therefore, be very useful on the characterization of tissues and the spatial relation between cell structures. The automation of the histological image analysis helps removing the current issues related to the inherent subjectivity associated with the observers, and time spent on repetitive and monotonous tasks. The three dimensional reconstruction of these histological images, on the other hand, allows to have a high resolution volume of the tissue to be analyzed.

The histological image analysis main focus is the automation of laboratory procedures that are subjective and repetitive and also improve user's analysis and visualization of histological slides. For that, it was developed a series of algorithms that are capable of aligning a set of images and performing their analysis. Part of those algorithms is the image alignment algorithm, used to align the sets of images; the stain separation algorithm, to separate the different colors that are present in an histological image, as a result of its staining; and segmentation algorithms, in order to obtain total content of elastin and collagen of each image.

The image alignment algorithm was developed with success, however there are some key factors that influence its performance. The quality of the tissue slices is crucial to the outcome of this algorithm. If the tissue is cut or distorted the results of the alignment will be affected. Another important issue is the presence of guide zones that will enable the alignment of the set of images. This zones have to be intact in order to allow a good computation of its centroids, otherwise the centroids position will be inaccurate and the alignment will have some errors.

The stain separation and segmentation algorithms also showed good results, when compared to the results obtained through a manual segmentation. The success of these algorithms depend on an uniform illumination of the input images.

The main purpose of the three dimensional analysis was to reconstruct, in 3D, a tissue segment from histological images. After this 3D reconstruction followed the estimation of the percentages of collagen and elastin. Later the amount of tissue component determined by the two dimension analysis was compared to the 3D volume to conclude if there is any kind of correlation between the 2D and 3D analysis.

The results for the three dimensional reconstruction were not the expected, since the reconstructions were very coarse. Part of this outcome can be explained by the used spacing between slices, which can cause significant differences in the next slice with respect to the previous slice. Possible small misalignment of the images can also lead to larger distances in the x and y directions, causing the unsuccessful reconstructions. As the results were not successful, the comparison between the volumes obtained through the 3D reconstruction and the volumes for the estimation from the 2D images was not possible to archive.

As future work, it would be interesting to compare the results of the automatic segmentation with the results of the manual segmentation performed by specialists. This would increase the reliability of the obtained results. The current stain separation algorithm performs the separation of Miller's Elastic Staining. It would also be interesting to add and test new stainings, such as Hematoxylin and eosin staining, for example. As for the 3D reconstruction, it was used slices with the spacing between slices twice the slice thickness and, it is possible to obtain slices with the slice thickness equal to the spacing between slice. Testing this possibility will allow a better understanding of the reasons behind the obtained results, and hopefully, to archive successfully 3D reconstructing.

References

[1] Fatma El-Zahraa Ahmed El-Gamal, Mohammed Elmogy, and Ahmed Atwan. Current trends in medical image registration and fusion. *Egyptian Informatics Journal*, 17(1):99–124, 2016.

[2] Ayman S El-Baz, Rajendra Acharya, Majid Mirmehdi, and Jasjit S Suri. *Multi modality state-of-the-art medical image segmentation and registration methodologies*, volume 1. Springer Science & Business Media, 2011.

[3] Christopher C Conlin, Jeff L Zhang, Florian Rousset, Clement Vachet, Yangyang Zhao, Kathryn A Morton, Kristi Carlston, Guido Gerig, and Vivian S Lee. Performance of an efficient image-registration algorithm in processing mr renography data. *Journal of Magnetic Resonance Imaging*, 43(2):391–397, 2016.

[4] PJ Tadrous. Digital stain separation for histological images. *Journal of microscopy*, 240(2):164–172, 2010.

[5] Nida M Zaitoun and Musbah J Aqel. Survey on image segmentation techniques. *Procedia Computer Science*, 65:797–806, 2015.

[6] Rafael C Gonzalez, Richard E Woods, et al. *Digital image processing*. Prentice hall New Jersey, 2002.

[7] Zhihua Zhang. Artificial neural network. In *Multivariate Time Series Analysis in Climate and Environmental Research*, pages 1–35. Springer, 2018.

[8] microDimensions. Voloom - 3d histology software for reconstruction of serial sections. URL: https://micro-dimensions.com/voloom/.

[9] 3D Printing Industry. Materialise's heartprint(r) now listed as a class 1 medical device. URL: https://3dprintingindustry.com/news/materialise-heartprint-medical-3d-printing-34386/.

[10] Michael T McCann, Joshita Majumdar, Cheng Peng, Carlos A Castro, and Jelena Kovačević. Algorithm and benchmark dataset for stain separation in histology images. In *Image Processing (ICIP), 2014 IEEE International Conference on*, pages 3953–3957. IEEE, 2014.

[11] Fernando A. Ferrer. Chapter 49 - oncology principle of pediatric genitourinary tumors. In John P. Gearhart, Richard C. Rink, and Pierre D.E. Mouriquand, editors, *Pediatric Urology (Second Edition)*, pages 663 – 670. W.B. Saunders, Philadelphia, second edition edition, 2010.

[12] Alex Mejia, Stephanie Schulz, Terry Hyslop, David S Weinberg, and Scott A Waldman. Molecular staging estimates occult tumor burden in colorectal cancer. In *Advances in clinical chemistry*, volume 52, pages 19–39. Elsevier, 2010.

[13] Wilbur A. Franklin, Dara L. Aisner, Miriam D. Post, Paul A. Bunn, and Marileila Varella Garcia. 17 - pathology, biomarkers, and molecular diagnostics. In John E. Niederhuber, James O. Armitage, James H. Doroshow, Michael B. Kastan, and Joel E. Tepper, editors, *Abeloff's Clinical Oncology (Fifth Edition)*, pages 226 – 252.e6. Content Repository Only!, Philadelphia, fifth edition edition, 2014.

[14] AD Belsare and MM Mushrif. Histopathological image analysis using image processing techniques: An overview. *Signal & Image Processing*, 3(4):23, 2012.

[15] Torstein R Meling, Siril G Rogne, and Eirik Helseth. Melanoma metastases are underrepresented in cerebellum compared with metastases from colorectal cancers. In *Brain Metastases from Primary Tumors, Volume 3*, pages 37–48. Elsevier, 2016.

[16] Elizabeth L Hedberg, Henriette C Kroese-Deutman, Charles K Shih, Jeremy J Lemoine, Michael AK Liebschner, Michael J Miller, Alan W Yasko, Roger S Crowther, Darrell H Carney, Antonios G Mikos, et al. Methods: a comparative analysis of radiography, microcomputed tomography, and histology for bone tissue engineering. *Tissue Engineering*, 11(9-10):1356–1367, 2005.

[17] Morten Ladekarl. Objective malignancy grading: a review emphasizing unbiased stereology applied to breast tumors. *Apmis*, 106(S79):5–34, 1998.

[18] William C Allsbrook, Kathy A Mangold, Maribeth H Johnson, Roger B Lane, Cynthia G Lane, and Jonathan I Epstein. Interobserver reproducibility of gleason grading of prostatic carcinoma: general pathologist. *Human pathology*, 32(1):81–88, 2001.

[19] Metin N Gurcan, Laura E Boucheron, Ali Can, Anant Madabhushi, Nasir M Rajpoot, and Bulent Yener. Histopathological image analysis: A review. *IEEE reviews in biomedical engineering*, 2:147–171, 2009.

[20] Navid Farahani, Anil V Parwani, and Liron Pantanowitz. Whole slide imaging in pathology: advantages, limitations, and emerging perspectives. *Pathol Lab Med Int*, 7:23–33, 2015.

[21] Jean R Slutsky and Carolyn M Clancy. Ahrq's effective health care program: why comparative effectiveness matters. *American Journal of Medical Quality*, 24(1):67–70, 2009.

[22] Shaimaa Al-Janabi, André Huisman, Aryan Vink, Roos J Leguit, G Johan A Offerhaus, Fiebo JW Ten Kate, Marijke R Van Dijk, and Paul J Van Diest. Whole slide images for primary diagnostics in dermatopathology: a feasibility study. *Journal of clinical pathology*, pages jclinpath–2011, 2011.

[23] Patricia Switten Nielsen, Jan Lindebjerg, Jan Rasmussen, Henrik Starklint, Marianne Waldstrøm, and Bjarne Nielsen. Virtual microscopy: an evaluation of its validity and diagnostic performance in routine histologic diagnosis of skin tumors. *Human pathology*, 41(12):1770–1776, 2010.

[24] Guilherme F Caetano, Marcio Fronza, Marcel N Leite, Ary Gomes, and Marco Andrey Cipriani Frade. Comparison of collagen content in skin wounds evaluated by biochemical assay and by computer-aided histomorphometric analysis. *Pharmaceutical biology*, 54(11):2555–2559, 2016.

[25] Jennifer M Milner and Tim E Cawston. Matrix metalloproteinase knockout studies and the potential use of matrix metalloproteinase inhibitors in the rheumatic diseases. *Current Drug Targets-Inflammation & Allergy*, 4(3):363–375, 2005.

[26] TA Wynn. Cellular and molecular mechanisms of fibrosis. *The Journal of pathology*, 214(2):199–210, 2008.

[27] Barbara Shih, Elloise Garside, Duncan Angus McGrouther, and Ardeshir Bayat. Molecular dissection of abnormal wound healing processes resulting in keloid disease. *Wound repair and regeneration*, 18(2):139–153, 2010.

[28] Marco Andrey Cipriani Frade, Rodolfo Vieira Valverde, Raimunda Violante Campos De Assis, Joaquim Coutinho-Netto, and Norma T Foss. Chronic phlebopathic cutaneous ulcer: a therapeutic proposal. *International journal of dermatology*, 40(3):238–240, 2001.

[29] Yung-Kai Lin and Che-Yung Kuan. Development of 4-hydroxyproline analysis kit and its application to collagen quantification. *Food chemistry*, 119(3):1271–1277, 2010.

[30] Yi Song, Darren Treanor, Andrew J Bulpitt, and Derek R Magee. 3d reconstruction of multiple stained histology images. *Journal of pathology informatics*, 4(Suppl), 2013.

[31] Sébastien Ourselin, Alexis Roche, Gérard Subsol, Xavier Pennec, and Nicholas Ayache. Reconstructing a 3d structure from serial histological sections. *Image and vision computing*, 19(1):25–31, 2001.

[32] Habibiollah Danyali and Alfred Mertins. Volumetric medical image coding: an object-based, lossy-to-lossless and fully scalable approach. *Journal of medical signals and sensors*, 1(1):1, 2011.

[33] U-D Braumann, J-P Kuska, Jens Einenkel, L-C Horn, Markus Loffler, and Michael Hockel. Three-dimensional reconstruction and quantification of cervical carcinoma invasion fronts from histological serial sections. *IEEE Transactions on Medical Imaging*, 24(10):1286–1307, 2005.

[34] Frederik Maes, Andre Collignon, Dirk Vandermeulen, Guy Marchal, and Paul Suetens. Multimodality image registration by maximization of mutual information. *IEEE transactions on Medical Imaging*, 16(2):187–198, 1997.

[35] Derek LG Hill, Philipp G Batchelor, Mark Holden, and David J Hawkes. Medical image registration. *Physics in medicine & biology*, 46(3):R1, 2001.

[36] Stefan Klein, Marius Staring, Keelin Murphy, Max A Viergever, and Josien PW Pluim. Elastix: a toolbox for intensity-based medical image registration. *IEEE transactions on medical imaging*, 29(1):196–205, 2010.

[37] JB Antoine Maintz and Max A Viergever. A survey of medical image registration. *Medical image analysis*, 2(1):1–36, 1998.

[38] Delphine Plattard, Marine Soret, Jocelyne Troccaz, Patrick Vassal, Jean-Yves Giraud, Guillaume Champleboux, Xavier Artignan, and Michel Bolla. Patient set-up using portal images: 2d/2d image registration using mutual information. *Computer Aided Surgery*, 5(4):246–262, 2000.

[39] Jean-Philippe Thirion. Extremal points: definition and application to 3d image registration. In *CVPR*, pages 587–592, 1994.

[40] Dongshan Fu and Gopinath Kuduvalli. A fast, accurate, and automatic 2d–3d image registration for image-guided cranial radiosurgery. *Medical physics*, 35(5):2180–2194, 2008.

[41] Torsten Rohlfing, Daniel B Russakoff, Martin J Murphy, and Calvin R Maurer. Intensity-based registration algorithm for probabilistic images and its application for 2d to 3d image registration. In *Medical Imaging 2002: Image Processing*, volume 4684, pages 581–592. International Society for Optics and Photonics, 2002.

[42] Jacques Feldmar, Nicholas Ayache, and Fabienne Betting. 3d-2d projective registration of free-form curves and surfaces. In *Computer Vision, 1995. Proceedings., Fifth International Conference on*, pages 549–556. IEEE, 1995.

[43] Vidya Bhat, Shyamsunder N Bhat, and H Anitha. Accelerated digitally reconstructed radiograph generation scheme for 2d to 3d image registration of vertebrae based on sparse sampling and multi-resolution. 2017.

[44] A Ghaffari and E Fatemizadeh. Mono-modal image registration via correntropy measure. In *Machine Vision and Image Processing (MVIP), 2013 8th Iranian Conference on*, pages 223–226. IEEE, 2013.

[45] Yuanjie Zheng, Ebenezer Daniel, Allan A Hunter, Rui Xiao, Jianbin Gao, Hongsheng Li, Maureen G Maguire, David H Brainard, and James C Gee. Landmark matching based retinal image alignment by enforcing sparsity in correspondence matrix. *Medical image analysis*, 18(6):903–913, 2014.

[46] Ali Can, Charles V. Stewart, Badrinath Roysam, and Howard L. Tanenbaum. A feature-based, robust, hierarchical algorithm for registering pairs of images of the curved human retina. *IEEE transactions on pattern analysis and machine intelligence*, 24(3):347–364, 2002.

[47] Marius Erdt, Sebastian Steger, and Georgios Sakas. Regmentation: A new view of image segmentation and registration. *Journal of Radiation Oncology Informatics*, 4(1):1–23, 2017.

[48] Xin Peng, Qiang Chen, and Benzheng Wei. An efficient medical image registration method based on mutual information model. In *Fuzzy Systems and Knowledge Discovery (FSKD), 2010 Seventh International Conference on*, volume 5, pages 2168–2172. IEEE, 2010.

[49] John L Rubinstein and Marcus A Brubaker. Alignment of cryo-em movies of individual particles by optimization of image translations. *Journal of Structural Biology*, 192(2):188–195, 2015.

[50] Csaba Domokos and Zoltan Kato. Affine shape alignment using covariant gaussian densities: A direct solution. *Journal of Mathematical Imaging and Vision*, 51(3):385–399, 2015.

[51] Kawal S Rhode, Derek LG Hill, Philip J Edwards, John Hipwell, Daniel Rueckert, Gerardo Sanchez-Ortiz, Sanjeet Hegde, Vithuran Rahunathan, and Reza Razavi. Registration and tracking to integrate x-ray and mr images in an xmr facility. *IEEE transactions on medical imaging*, 22(11):1369–1378, 2003.

[52] HM Chan, Albert CS Chung, Simon CH Yu, and WMIII Wells. 2d-3d vascular registration between digital subtraction angiographic (dsa) and magnetic resonance angiographic (mra) images. In *Biomedical Imaging: Nano to Macro, 2004. IEEE International Symposium on*, pages 708–711. IEEE, 2004.

[53] Alexander Wong and William Bishop. Indirect knowledge-based approach to non-rigid multi-modal registration of medical images. In *Electrical and Computer Engineering, 2007. CCECE 2007. Canadian Conference on*, pages 1175–1178. IEEE, 2007.

[54] Jonathan Rohrer and Leiguang Gong. Focused atlas-based image registration for recognition. In *Image Processing, 2008. ICIP 2008. 15th IEEE International Conference on*, pages 1808–1811. IEEE, 2008.

[55] Wei-Yen Hsu. A novel image registration algorithm for indoor and built environment applications. *Computer-Aided Civil and Infrastructure Engineering*, 30(10):802–814, 2015.

[56] PJ Tadrous. *The imaging of benign and malignant breast tissue by fluorescence lifetime imaging and optical coherence tomography*. PhD thesis, University of London (Imperial College), 2003.

[57] Arnout C Ruifrok, Dennis A Johnston, et al. Quantification of histochemical staining by color deconvolution. *Analytical and quantitative cytology and histology*, 23(4):291–299, 2001.

[58] Jeroen AWM Van der Laak, Martin MM Pahlplatz, Antonius GJM Hanselaar, and Peter de Wilde. Hue-saturation-density (hsd) model for stain recognition in digital images from transmitted light microscopy. *Cytometry Part A*, 39(4):275–284, 2000.

[59] Devrim Onder, Selen Zengin, and Sulen Sarioglu. A review on color normalization and color deconvolution methods in histopathology. *Applied Immunohistochemistry & Molecular Morphology*, 22(10):713–719, 2014.

[60] Marc Macenko, Marc Niethammer, JS Marron, David Borland, John T Woosley, Xiaojun Guan, Charles Schmitt, and Nancy E Thomas. A method for normalizing histology slides for quantitative analysis. In *Biomedical Imaging: From Nano to Macro, 2009. ISBI'09. IEEE International Symposium on*, pages 1107–1110. IEEE, 2009.

[61] Yi-Ying Wang, Shao-Chien Chang, Li-Wha Wu, Sen-Tien Tsai, and Yung-Nien Sun. *A color-based approach for automated segmentation in tumor tissue classification*. 2007.

[62] Vagelis Hristidis. *Information discovery on electronic health records*. CRC Press, 2009.

[63] Ashish Kumar Bhandari, Anil Kumar, and Girish Kumar Singh. Modified artificial bee colony based computationally efficient multilevel thresholding for satellite image segmentation using kapur's, otsu and tsallis functions. *Expert Systems with Applications*, 42(3):1573–1601, 2015.

[64] Nikita Sharma, Mahendra Mishra, and Manish Shrivastava. Colour image segmentation techniques and issues: an approach. *International Journal of Scientific & Technology Research*, 1(4):9–12, 2012.

[65] KA Abdul Nazeer and MP Sebastian. Improving the accuracy and efficiency of the k-means clustering algorithm. In *Proceedings of the world congress on engineering*, volume 1, pages 1–3, 2009.

[66] Mahipal Singh Choudhry and Rajiv Kapoor. Performance analysis of fuzzy c-means clustering methods for mri image segmentation. *Procedia Computer Science*, 89:749–758, 2016.

[67] Xuanli Lisa Xie and Gerardo Beni. A validity measure for fuzzy clustering. *IEEE Transactions on pattern analysis and machine intelligence*, 13(8):841–847, 1991.

[68] Menglong Xu, Dong Zhang, Yan Yang, Yu Liu, Zhiyong Yuan, and Qianqing Qin. A split-and-merge-based uterine fibroid ultrasound image segmentation method in hifu therapy. *PloS one*, 10(5):e0125738, 2015.

[69] Akanksha Bali and Shailendra Narayan Singh. A review on the strategies and techniques of image segmentation. In *Advanced Computing & Communication Technologies (ACCT), 2015 Fifth International Conference on*, pages 113–120. IEEE, 2015.

[70] Sirshendu Hore, Souvik Chakraborty, Sankhadeep Chatterjee, Nilanjan Dey, Amira S Ashour, Le Van Chung, and Dac-Nhuong Le. An integrated interactive technique for image segmentation using stack based seeded region growing and thresholding. *International Journal of Electrical and Computer Engineering*, 6(6):2773, 2016.

[71] Claudia I Gonzalez, Patricia Melin, Juan R Castro, Olivia Mendoza, and Oscar Castillo. An improved sobel edge detection method based on generalized type-2 fuzzy logic. *Soft Computing*, 20(2):773–784, 2016.

[72] Rajesh Mehra Nisha and Lalita Sharma. Comparative analysis of canny and prewitt edge detection techniques used in image processing. *International Journal of Engineering Trends and Technology (IJETT)*, 28(1):48–53, 2015.

[73] Anphy Jose, K Deepa Merlin Dixon, Naiji Joseph, E Silpa George, and V Anjitha. Performance study of edge detection operators. In *Embedded Systems (ICES), 2014 International Conference on*, pages 7–11. IEEE, 2014.

[74] Lijun Ding and Ardeshir Goshtasby. On the canny edge detector. *Pattern Recognition*, 34(3):721–725, 2001.

[75] materialize. Materialise mimics. URL: http://www.materialise.com/en/medical/software/mimics.

[76] Rushin Shojaii, Stephanie Bacopulos, Wenyi Yang, Tigran Karavardanyan, Demetri Spyropoulos, Afshin Raouf, Anne Martel, and Arun Seth. Reconstruction of 3-dimensional histology volume and its application to study mouse mammary glands. *Journal of visualized experiments: JoVE*, (89), 2014.

[77] Fritjof Helmchen and Winfried Denk. Deep tissue two-photon microscopy. *Nature methods*, 2(12):932, 2005.

[78] Thomy Mertzanidou, John H Hipwell, Sara Reis, David J Hawkes, Babak Ehteshami Bejnordi, Mehmet Dalmis, Suzan Vreemann, Bram Platel, Jeroen Laak, Nico Karssemeijer, et al. 3d volume reconstruction from serial breast specimen radiographs for mapping between histology and 3d whole specimen imaging. *Medical physics*, 44(3):935–948, 2017.

[79] Ramón Casero, Urszula Siedlecka, Elizabeth S Jones, Lena Gruscheski, Matthew Gibb, Jürgen E Schneider, Peter Kohl, and Vicente Grau. Transformation diffusion reconstruction of three-dimensional histology volumes from two-dimensional image stacks. *Medical image analysis*, 38:184–204, 2017.

[80] Johannes Streicher, Wolfgang J Weninger, and Gerd B Müller. External marker-based automatic congruencing: a new method of 3d reconstruction from serial sections. *The Anatomical Record*, 248(4):583–602, 1997.

[81] Mary E Booth, Darren Treanor, Nicholas Roberts, Derek R Magee, Valerie Speirs, and Andrew M Hanby. Three-dimensional reconstruction of ductal carcinoma in situ with virtual slides. *Histopathology*, 66(7):966–973, 2015.

[82] Stefan G Schalk, Arnoud Postema, Tamerlan A Saidov, Libertario Demi, Martijn Smeenge, Jean JMCH de la Rosette, Hessel Wijkstra, and Massimo Mischi. 3d surface-based registration of ultrasound and histology in prostate cancer imaging. *Computerized Medical Imaging and Graphics*, 47:29–39, 2016.

[83] Maik Stille, Edward J Smith, William R Crum, and Michel Modo. 3d reconstruction of 2d fluorescence histology images and registration with in vivo mr images: application in a rodent stroke model. *Journal of neuroscience methods*, 219(1):27–40, 2013.

[84] Materialise. *Mimics Student Edition Course Book*. Materialise.

[85] Yao-Jun Zhang, Hao Zhu, Shun-Yi Shi, Takashi Muramatsu, Dao-Rong Pan, Fei Ye, Jun-Jie Zhang, Nai-Liang Tian, Christos V Bourantas, and Shao-Liang Chen. Comparison between two-dimensional and three-dimensional quantitative coronary angiography for the prediction of functional severity in true bifurcation lesions: Insights from the randomized dk-crush ii, iii, and iv trials. *Catheterization and Cardiovascular Interventions*, 87(S1):589–598, 2016.

[86] Jan Hering, Frederik Bernd Laun, Wolfgang Lederer, Heidi Daniel, Tristan Anselm Kuder, Anne Stieber, Stefan Delorme, Klaus H Maier-Hein, Heinz-Peter Schlemmer, and Sebastian Bickelhaupt. Applicability and discriminative value of a semiautomatic three-dimensional spherical volume for the assessment of the apparent diffusion coefficient in suspicious breast lesions—feasibility study. *Clinical imaging*, 40(6):1280–1285, 2016.

[87] Sandra RR Tecelão, Jaco JM Zwanenburg, Joost Kuijer, Carel C de Cock, Tjeerd Germans, Albert C van Rossum, and J Tim Marcus. Quantitative comparison of 2d and 3d circumferential strain using mri tagging in normal and lbbb hearts. *Magnetic resonance in medicine*, 57(3):485–493, 2007.

[88] Wei Shen, Mark Punyanitya, ZiMian Wang, Dympna Gallagher, Marie-Pierre St-Onge, Jeanine Albu, Steven B Heymsfield, and Stanley Heshka. Visceral adipose tissue: relations between single-slice areas and total volume. *The American journal of clinical nutrition*, 80(2):271–278, 2004.

[89] MJ Firbank and A Coulthard. Evaluation of a technique for estimation of extraocular muscle volume using 2d mri. *The British journal of radiology*, 73(876):1282–1289, 2000.

[90] OPTIKA ITALY. Optiscan10. URL: http://www.optikamicroscopes.com/index.php?option=com_virtuemart&view=productdetails&virtuemart_product_id=904&virtuemart_category_id=6&lang=en.

[91] ImageJ. Fiji. URL: https://imagej.net/Fiji.